Research Square

Preprints are preliminary reports that have not undergone peer review.
They should not be considered conclusive, used to inform clinical practice,
or referenced by the media as validated information.

Sliding-Mode Lyapunov Redesign for Fault-Tolerant Control of Morphing Aircraft with Actuator Faults

Hao HE

hastur2024@163.com

National University of Defense Technology

Peng WANG

National University of Defense Technology

Guojian TANG

National University of Defense Technology

Research Article

Keywords: Morphing aircraft, Fault-tolerant control, Sliding-mode control, Lyapunov redesign

Posted Date: November 19th, 2026

DOI: https://doi.org/10.21203/rs.3.rs-11525646/v1

License: This work is licensed under a Creative Commons Attribution 4.0 International License.
Read Full License

Additional Declarations: No competing interests reported.

Sliding-Mode Lyapunov Redesign for Fault-Tolerant Control of Morphing Aircraft with Actuator Faults

Hao HE[1,2 *], **Peng WANG**[1,2], **Guojian TANG**[1,2]

1 College of Aerospace Science and Engineering, National University of Defense Technology, Changsha 410073, China.

2 State Key Laboratory of High-Efficiency Reusable Aerospace Transportation Technology, Changsha 410073, China.

Abstract

This paper focuses on the fault-tolerant control(FTC) problem of morphing aircraft with actuator faults. By integrating Lyapunov Redesign(LR) and Sliding-Mode Control(SMC), a novel Sliding-Mode Lyapunov Redesign(SMLR) framework for morphing aircraft under actuator faults is established. This framework integrates the strong robustness of SMC with the concise treatment of uncertainty in LR, providing a simple, effective, and theoretically rigorous FTC scheme. Firstly, a nominal system controller is designed based on finite-time control theory and backstepping control methods. Its finite-time stability is proven via Lyapunov theory. Then, a novel nonlinear sliding surface is proposed to ensure rapid and precise convergence of the LR key variables near the origin. Based on this sliding surface, a continuous sliding-mode fault-tolerant controller is developed. The designed controller achieves rapid attitude control and effective actuator fault suppression for the morphing aircraft. Furthermore, its Input-to-State Stability(ISS) is demonstrated via Lyapunov theory. Finally, several simulations validate the effectiveness and superior performance of the proposed method.

Keywords: Morphing aircraft; Fault-tolerant control; Sliding-mode control; Lyapunov redesign

*Corresponding author.

E-mail address: hastur2024@163.com (H. He), wonderful2035@163.com (P. Wang), tangguojian@nudt.edu.cn (G. Tang).

1. Introduction[1]

Morphing aircraft achieve superior aerodynamic performance and maneuverability through local or global shape changes, enabling optimal control across complex flight environments and diverse mission scenarios [1],[2]. Research in this field covers aeroelastic dynamic models [3], morphing-induced aerodynamic stability [4],[5], and additional forces and moments generated during shape changes under a multibody assumption. These shape changes make the aerodynamics more complex and variable than those of conventional fixed-wing aircraft [6]. As a result, morphing aircraft face greater fault risks [7],[8]. Therefore, fault-tolerant control (FTC) for morphing aircraft under potential failures is the primary focus of this research.

FTC has been a prominent research area over the past decades, focused on maintaining stability and flight control

performance despite system failures [9], making it crucial for system reliability and safety. Based on whether fault detection and diagnosis is performed, FTC can be divided into active fault-tolerant control (AFTC) [10],[11] and passive fault-tolerant control(PFTC) [12],[13]. Morphing aircraft typically encounter sensor faults [14],[15], internal system faults [16], and actuator faults [17],[18],[19].

AFTC can achieve high performance through explicit fault estimation and compensation, but its dependence on fault detection poses challenges for morphing aircraft: the highly time-varying dynamics during morphing increase the risk of false alarms and missed detections, and inherent diagnostic delays may leave the most critical transient phase insufficiently compensated. PFTC avoids these issues by providing instant robust compensation without fault detection, making it particularly suitable for abrupt actuator faults during shape transition. Motivated by this, we develop a PFTC framework that integrates sliding-mode control with Lyapunov redesign (LR).

LR, first proposed by Leitman [20] and Gutman [21], has been widely applied to address uncertainty in nonlinear control systems. The main idea is to separate the uncertainty effects from the nominal system via Lyapunov stability analysis, then incorporate a feedback control term targeting the uncertainty into the nominal control scheme, thereby achieving control of the entire system. This approach is highly effective for handling matching uncertainties. The classical LR method employed only a discontinuous unit control term. While it achieved excellent stabilization performance under known uncertainty bounds and disturbance upper bounds, it produced discontinuous control signals. In subsequent years, continuous feedback control methods were also developed [22],[23]. Recently, LR has been revisited due to its simplicity in handling uncertainty and its strong robustness.

The latest LR research has focused on extending its application beyond nonlinear systems. Extensive studies have covered linearized systems with parameter uncertainties [24], linear systems with input and state delays [25], multi-agent systems with dynamic uncertainties [26], and single-degree-of-freedom structural systems [27]. Diverse forms of uncertainty aligned with engineering practice have also been considered. Effective measures have also been proposed to address the discontinuity and pronounced chattering inherent in classical LR control signals. Combining boundary layer design with feedback control term processing offers a concise and effective approach to mitigate chattering while ensuring system convergence [28],[29],[30]. Under this design, the system exhibits input-to-state stability; if uncertainties remain bounded, their impact can be arbitrarily reduced but not completely eliminated.

Sliding Mode Control (SMC) is widely recognized for its robust performance and extensive design flexibility [31],**Error! Reference source not found.**,**Error! Reference source not found.**. It remains widely applied in nonlinear control system design, with higher-order sliding mode methods gaining popularity due to their enhanced robustness and superior chattering suppression [34],[35].

The integration of LR and SMC is a current research focus. A common approach uses key variables in the LR model as sliding surfaces to design sliding mode controllers based on their dynamic characteristics [36]. Similarly, introducing higher-order sliding mode control algorithms [37],[38] on this basis can further suppress chattering. This approach has produced rich results and demonstrates superior algorithmic performance while addressing classical LR and SMC issues. However, most existing LR-SMC frameworks directly adopt key variables as sliding surfaces-a linear approach that slows near-origin convergence and causes severe chattering near the surface. For morphing aircraft, these issues worsen due to continuously varying aerodynamics and inertia during wing sweep transitions. The present work fills this gap by proposing a novel nonlinear sliding surface embedded within a continuous sliding-mode Lyapunov redesign framework that simultaneously accelerates near-origin convergence, suppress chattering, and ensures provable input-to-state stability for morphing vehicles subject to actuator faults.

To address prior limitations, this paper proposes an advanced nonlinear sliding surface that enhances convergence properties of key variables approaching the origin while ensuring control signal smoothness. Additionally, actuator faults in morphing aircraft manifest as matching uncertainties. Motivated by the above discussion, this paper aims to develop a sliding-mode Lyapunov redesign for fault-tolerant control of morphing aircraft under actuator faults. The main contributions are as follows.

1) Unlike conventional LR-based nominal controller designs that rely on asymptotic convergence or require complex gain tuning, we propose a finite-time nominal controller by integrating backstepping control with finite-time command filtering. This avoids the "differential explosion" problem inherent in standard backstepping and guarantees rapid convergence of the nominal system dynamics within a fixed time bound [39].

2) Prior methods adopt the key variable directly as a linear sliding surface, causing slow convergence near the origin and significant chattering. We construct a nonlinear surface that accelerates convergence of the key variable around the origin and inherently smooths the control signal. This design effectively mitigates the long-standing conflict between convergence and chattering suppression in classical LR-SMC schemes.

3) Most existing LR-based PFTC schemes produce discontinuous control signals or rely on simplified uncertainty bounds. Here, we establish a continuous sliding-mode fault-tolerant controller that integrates LR with a continuous smoothing controller. By incorporating boundary-layer smoothing functions and auxiliary dynamics, the resulting control law is continuously differentiable, eliminating high-frequency switching. Rigorous Input-to-State Stability (ISS) is proved using Lyapunov theory, showing that the closed-loop system remains stable under bounded actuator faults and disturbances.

4) Various simulations considering morphing process are designed to validate the effectiveness, superiority, and robustness of the proposed method. These include nominal controller simulations, fault-tolerant controller simulations under various faults, comparative simulations of different methods under identical faults, and program angle command simulations with coefficient perturbations.

2. Problem formulation

2.1. Attitude kinematical and dynamic models

The morphing aircraft differs from fixed-wing aircraft by including additional terms related to the moments caused by shape change. The attitude kinematical and dynamic models for the variable-sweep aircraft discussed in this paper are established.

$$\begin{cases} \dot{\alpha} = -\omega_x \cos\alpha \tan\beta + \omega_y \sin\alpha \tan\beta + \omega_z - \dfrac{1}{mV\cos\beta}\left(L - mg\cos\theta\cos\gamma_V\right) \\ \dot{\beta} = \omega_x \sin\alpha + \omega_y \cos\alpha + \dfrac{1}{mV}\left(N + mg\cos\theta\sin\gamma_V\right) \\ \dot{\gamma}_V = \omega_x \cos\alpha\sec\beta - \omega_y \sin\alpha\sec\beta + \dfrac{1}{mV}[(\tan\beta + \tan\theta\sin\gamma_V)L + N\tan\theta\cos\gamma_V \\ \quad + mg\cos\theta\tan\beta\sin\gamma_V] \end{cases} \tag{1}$$

$$\dot{\boldsymbol{\omega}} = \left(\boldsymbol{I}_b + \sum_{j=l,r}\boldsymbol{I}_{bj}\right)^{-1}\left(\boldsymbol{M}_c - \boldsymbol{M}_f - \sum_{j=l,r} m_j(\boldsymbol{r}_{O_m\to O_j} + \boldsymbol{r}_{O_j\to C_j})\times(\dot{\boldsymbol{v}} + \boldsymbol{\omega}\times\boldsymbol{v})\right) \tag{2}$$

The kinematical models of the morphing aircraft are denoted by the attack angle α, sideslip angle β and bank angle γ_v. And the dynamic models are denoted by the roll angle rate ω_x, yaw angle rate ω_y and pitch angle rate ω_z respectively. And m is the mass of aircraft, V and θ are flight velocity and flight path angle respectively. The aerodynamic forces are lift force L, drag force D, and lateral force N. The gravitational acceleration is denoted by g. The aerodynamic forces and moments $\boldsymbol{M}_c$ are expressed as follows.

$$\begin{bmatrix} L \\ D \\ N \end{bmatrix} = \frac{1}{2}\rho V^2 S_0 \begin{bmatrix} C_L \\ C_D \\ C_N \end{bmatrix}, \boldsymbol{M}_c = \begin{bmatrix} M_{cx} \\ M_{cy} \\ M_{cz} \end{bmatrix} = \frac{1}{2}\rho v^2 S_0 L_0 \begin{bmatrix} m_x \\ m_y \\ m_z \end{bmatrix} \tag{3}$$

Where ρ is atmospheric density, S_0 is the aerodynamic reference area, L_0 is the aerodynamic reference length.

L, D and N are the lift force, drag force, and lateral force, respectively. C_D, C_L and C_N are the nominal aerodynamic drag, lift, and lateral force coefficients. m_x, m_y and m_z are roll moment coefficient, yaw moment coefficient and pitch moment coefficient. The equivalent aerodynamic force and moment coefficients calculation model are displayed in section 2.2.

In Eq. (2), $\boldsymbol{I}_b$ denotes the moment of inertia of the aircraft body, $\boldsymbol{I}_{bj}$ denotes the moment of inertia of the aircraft wing which can be expressed as

$$\boldsymbol{I}_{\mathrm{bj}} = -m_j \boldsymbol{r}^{\times}_{O_m \to O_j} \boldsymbol{r}^{\times}_{O_m \to O_j} - m_j \boldsymbol{R}_{bj} \boldsymbol{r}^{\times}_{O_j \to C_j} \boldsymbol{R}^T_{bj} \boldsymbol{r}^{\times}_{O_m \to O_j} - m_j \boldsymbol{r}^{\times}_{O_m \to O_j} \boldsymbol{R}_{bj} \boldsymbol{r}^{\times}_{O_j \to C_j} \boldsymbol{R}^T_{bj} + \boldsymbol{R}_{bj} \boldsymbol{I}_j \boldsymbol{R}^T_{bj} \tag{4}$$

Where m_j is the mass of aircraft wing, $\boldsymbol{r}_{O_m \to O_j}$ denotes the rotation vector of aircraft body relative to aircraft wing in the body coordinate system, $\boldsymbol{r}^{\times}_{O_m \to C_j}$ denotes the skew-symmetric matrix. $\boldsymbol{r}_{O_j \to C_j}$ denotes the rotation vector of aircraft body relative to aircraft wing in the aircraft wing coordinate system, $\boldsymbol{r}^{\times}_{O_j \to C_j}$ denotes the skew-symmetric matrix. l, r denotes the left wing and the right wing respectively. $\boldsymbol{R}_{\mathrm{bj}}$ denotes the rotation matrix from the aircraft wing coordinate system to the body coordinate system, which is expressed as

$$\begin{cases} \boldsymbol{R}_{\mathrm{bl}} = (\boldsymbol{M}_2(90^\circ + \chi_l))^T \\ \boldsymbol{R}_{\mathrm{br}} = (\boldsymbol{M}_2(-90^\circ - \chi_r))^T \end{cases} \tag{5}$$

Where $\boldsymbol{M}_2$ is the rotation matrix of y-axis, χ denotes the sweep angle of the morphing aircraft.

In Eq. (2), $\boldsymbol{M}_f$ is the dynamic forces caused by morphing wing, which is expressed as

$$\begin{aligned} \boldsymbol{M}_f = {} & \boldsymbol{\omega}_b \times (\boldsymbol{I}_b \boldsymbol{\omega}_b) + \sum_{j=l,r} \boldsymbol{I}^b_j \dot{\boldsymbol{\omega}}_j + \\ & \sum_{j=l,r} m_j \boldsymbol{r}_{O_m \to O_j} \times (\boldsymbol{\omega}_b \times (\boldsymbol{\omega}_b \times \boldsymbol{r}_{O_m \to O_j})) + \\ & \sum_{j=l,r} m_j \boldsymbol{r}_{O_j \to C_j} \times (\boldsymbol{\omega}_b \times (\boldsymbol{\omega}_b \times \boldsymbol{r}_{O_m \to O_j})) + \\ & \sum_{j=l,r} m_j \boldsymbol{r}_{O_m \to O_j} \times ((\boldsymbol{\omega}_b + \boldsymbol{\omega}_j) \times ((\boldsymbol{\omega}_b + \boldsymbol{\omega}_j) \times \boldsymbol{r}_{O_j \to C_j})) + \\ & \sum_{j=l,r} (\boldsymbol{\omega}_b + \boldsymbol{\omega}_j) \times (\boldsymbol{I}^b_j (\boldsymbol{\omega}_b + \boldsymbol{\omega}_j)) + \\ & \sum_{j=l,r} m_j \boldsymbol{r}_{O_m \to O_j} \times (\boldsymbol{\omega}_j \times \boldsymbol{r}_{O_j \to C_j}) \end{aligned} \tag{6}$$

Where $\boldsymbol{\omega}_b$ is the angular rates vector about the aircraft's center of mass O_m in the body coordinate system. $\boldsymbol{\omega}_j$ denotes the rotation angular rates vector of the wing.

2.2. Aerodynamic models

Morphing aircraft have different aerodynamic performance compared with the fixed aircraft. In this paper, we study a morphing aircraft with variable swept-back angle. Therefore, the aerodynamic parameters including lift coefficient C_L, drag coefficient C_D, lateral coefficient C_N, roll moment coefficient m_x, yaw moment coefficient m_y and pitch moment coefficient m_z -must account for the aircraft's morphing characteristics. Unlike aerodynamic models of fixed-wing aircraft, inspired by ref. [40], aerodynamic models of the morphing aircraft should incorporate Mach number Ma, attack angle α, sideslip angle β, roll fin deflection δ_x, yaw fin deflection δ_y, pitch fin deflection δ_z and swept-back angle χ.

In this paper, the expression of the aerodynamic coefficients is obtained by polynomial fitting as

$$\begin{cases} C_L = \boldsymbol{C}^{\alpha}_L(Ma, \chi) \cdot \boldsymbol{\alpha}_L + \boldsymbol{C}^{\delta}_L(Ma, \alpha) \cdot \boldsymbol{\delta}_L \\ C_D = \boldsymbol{C}^{\alpha}_D(Ma, \chi) \cdot \boldsymbol{\alpha}_D + \boldsymbol{C}^{\delta}_D(Ma, \alpha) \cdot \boldsymbol{\delta}_D \\ C_N = \boldsymbol{C}^{\beta}_N(Ma, \chi) \cdot \boldsymbol{\beta}_N + \boldsymbol{C}^{\delta}_N(Ma, \alpha) \cdot \boldsymbol{\delta}_N \\ m_x = m^{\beta}_x(Ma, \chi) \cdot \beta + \boldsymbol{m}^{\delta}_x(Ma, \alpha) \cdot \boldsymbol{\delta}_{mx} + m^{\omega_x}_x(Ma, \chi) \cdot (\omega_x L_0 / v) \\ m_y = m^{\beta}_y(Ma, \chi) \cdot \beta + \boldsymbol{m}^{\delta}_y(Ma, \alpha) \cdot \boldsymbol{\delta}_{my} + m^{\omega_y}_y(Ma, \chi) \cdot (\omega_y L_0 / v) \\ m_z = m^{\chi}_z(Ma, \chi, \alpha) - \boldsymbol{m}^{\delta}_z(Ma, \alpha) \cdot \boldsymbol{\delta}_{mz} + m^{\omega_y}_z(Ma, \chi) \cdot (\omega_z L_0 / v) \end{cases} \tag{7}$$

Where all vectors like $\boldsymbol{\alpha},\boldsymbol{\beta}$ and $\boldsymbol{\delta}$ are vectors of attack angle, sideslip angle and rudder deflection angles. Each vector is composed of the following specific expressions as

$$\begin{cases} \boldsymbol{\alpha}_L = \begin{bmatrix} \alpha & 1 \end{bmatrix}^T, \boldsymbol{\delta}_L = \begin{bmatrix} \delta_z \end{bmatrix}^T \\ \boldsymbol{\alpha}_D = \begin{bmatrix} \alpha^2 & \alpha & 1 \end{bmatrix}^T, \boldsymbol{\delta}_D = \begin{bmatrix} \delta_x^2 & \delta_z^2 \end{bmatrix}^T \\ \boldsymbol{\beta}_N = \begin{bmatrix} \beta & 1 \end{bmatrix}^T, \boldsymbol{\delta}_N = \begin{bmatrix} \delta_y \end{bmatrix}^T \\ \boldsymbol{\delta}_{mx} = \begin{bmatrix} \delta_x \end{bmatrix}^T, \boldsymbol{\delta}_{my} = \begin{bmatrix} \delta_y \end{bmatrix}^T, \boldsymbol{\delta}_{mz} = \begin{bmatrix} \delta_z \end{bmatrix}^T \end{cases} \tag{8}$$

In Eq. (7), matrixes $\boldsymbol{C}_i^k$ and $\boldsymbol{m}_j^k$ are coefficient matrixes of force coefficients and moment coefficients where i represents the force types like L, D, N and j represents the moments directions like x, y, z. Besides, k represents the variables such as $\delta_x, \delta_y, \delta_z, \alpha, \beta$. Ma, χ and α denote that they are contained in the coefficient matrix $\boldsymbol{C}_i^k$ and $\boldsymbol{m}_j^k$. Additionally, the concept of morphing ratio ξ is subsequently introduced to describe morphing degree.

$$\xi = \frac{\chi - \chi_{\min}}{\chi_{\max} - \chi_{\min}} \times 100\% \tag{9}$$

Where $\chi_{\max} = 70^\circ$ and $\chi_{\min} = 20^\circ$ denote the max maximum and minimum values of swept-back angle. The aerodynamic coefficients given in Eq. (7) are obtained by polynomial fitting over the entire operational range of sweep angle χ (from 20° to 70°). Therefore, the model is continuously valid and physically consistent for any intermediate configuration and both morphing directions.

2.3. Control-oriented models

The control-oriented models of morphing aircraft with actuator faults are expressed as

$$\begin{cases} \dot{\boldsymbol{x}}_1 = \boldsymbol{f}_1 + \boldsymbol{g}_1 \boldsymbol{x}_2 \\ \dot{\boldsymbol{x}}_2 = \boldsymbol{f}_2 + \boldsymbol{g}_2 \left(\boldsymbol{\tau u} + \boldsymbol{\upsilon} \right) \end{cases} \tag{10}$$

The state matrices are detailed as follows.

$$\boldsymbol{f}_1 = \begin{bmatrix} \dfrac{-L + mg\cos\theta\cos\gamma_V}{mV\cos\beta} \\ \dfrac{N + mg\cos\theta\sin\gamma_V}{mV} \\ \dfrac{(\tan\beta + \tan\theta\sin\gamma_V)L + N\tan\theta\cos\gamma_V}{mV} + \dfrac{g\cos\theta\tan\beta\sin\gamma_V}{V} \end{bmatrix} \tag{11}$$

$$\boldsymbol{g}_1 = \begin{bmatrix} -\cos\alpha\tan\beta & \sin\alpha\tan\beta & 1 \\ \sin\alpha & \cos\alpha & 0 \\ \cos\alpha\sec\beta & -\sin\alpha\sec\beta & 0 \end{bmatrix} \tag{12}$$

$$\boldsymbol{g}_2 = \frac{1}{2}\rho v^2 S_0 L_0 (\boldsymbol{I}_b + \sum_{j=l,r} \boldsymbol{I}_{bj})^{-1} \begin{bmatrix} m_x^{\delta_x} & 0 & 0 \\ 0 & m_y^{\delta_y} & 0 \\ 0 & 0 & m_z^{\delta_z} \end{bmatrix} \tag{13}$$

$$\boldsymbol{f}_2 = (\boldsymbol{I}_b + \sum_{j=l,r} \boldsymbol{I}_{bj})^{-1} [-\boldsymbol{M}_f - \sum_{j=l,r} m_j (\boldsymbol{r}_{O_m \to O_j} + \boldsymbol{r}_{O_j \to C_j}) \times (\dot{\boldsymbol{v}} + \boldsymbol{\omega} \times \boldsymbol{v})] \tag{14}$$

In Eq. (10), $\boldsymbol{x}_1 = \begin{bmatrix} \alpha & \beta & \gamma_v \end{bmatrix}^T$, $\boldsymbol{x}_2 = \begin{bmatrix} \omega_x & \omega_y & \omega_z \end{bmatrix}^T$ and $\boldsymbol{u} = \begin{bmatrix} \delta_x & \delta_y & \delta_z \end{bmatrix}^T$. The fault models are expressed as $\boldsymbol{u}_r = \boldsymbol{\tau u} + \boldsymbol{\upsilon}$ in this paper. Where $\boldsymbol{u}_r$ denotes the real control output under actuator fault. $\tau_i \in (0,1], i = 1,2,3$ denotes the actuator control loss factor, $\upsilon_i, i = 1,2,3$ denotes the actuator control drift factor.

Assumption 1. The fault factors representing by $\boldsymbol{\tau} = diag(\tau_1, \tau_2, \tau_3), \boldsymbol{\upsilon} = \begin{bmatrix} \upsilon_1, \upsilon_2, \upsilon_3 \end{bmatrix}^T$ are bounded . And there exist constants τ_ω and υ_ω such that for all t and x

$$0 < \tau_\omega \le \left\| \boldsymbol{\tau}(t,\boldsymbol{x}) \right\| \le 1; 0 \le \left\| \boldsymbol{\upsilon}(t,\boldsymbol{x}) \right\| \le \upsilon_\omega \tag{15}$$

Remark 1. As indicated in Assumption 1, bounded faults are commonly assumed in related studies [36][37][38]. Note also that the faults are unknown but cannot be arbitrarily large. Moreover, the actuator does not fail completely, so the system remains fully actuated.

3. Sliding-Mode Lyapunov Redesign for Fault-Tolerant Control

3.1. Preparations

Before introducing Sliding-mode Lyapunov redesign(SMLR) proposed in this paper, we first introduce the definition of classical Lyapunov redesign and relative lemmas.

Definition 1 [20],[21]. (Lyapunov redesign): Considering the uncertain nonlinear system

$$\dot{x} = f(t,x) + G(t,x)\left[u + \delta(t,x,u)\right] \tag{16}$$

Where $x \in \mathbb{R}^n$ is the state, $u \in \mathbb{R}^n$ is the control input, $\delta(t,x,u) \in \mathbb{R}^n$ is a bounded absolutely continuous function caused by parameter uncertainty, external disturbances, or system faults. For the nominal system, assume there exists a stabilizing control law $u = \varphi(t,x)$ such that the closed-loop dynamics

$$\dot{x} = f(t,x) + G(t,x)\varphi(t,x) \tag{17}$$

is uniformly asymptotical stable. Further assuming that the Lyapunov function in Eq. (17) is known. And there exists a continuous and differentiable function $V(t,x)$ such that for all $(t,x) \in [0,\infty) \times \boldsymbol{D}$ ($\boldsymbol{D} \subset \mathbb{R}^n$ is the domain containing the origin) satisfies the inequality

$$\begin{gathered} \alpha_1(\|x\|) \le V(t,x) \le \alpha_2(\|x\|) \\ \frac{\partial V}{\partial t} + \frac{\partial V}{\partial x}\left[f(t,x) + G(t,x)\varphi(t,x)\right] \le -\alpha_3(\|x\|) \end{gathered} \tag{18}$$

Where α_1, α_2 and α_3 are class K functions. Assume that when $u = \varphi(t,x) + v$ and δ satisfy

$$\left\| \delta(t,x,\varphi(t,x)+v) \right\| \le \rho(t,x) + \kappa_0 \|v\|, 0 \le \kappa_0 < 1 \tag{19}$$

Where $\rho(t,x) : [0,\infty) \times \boldsymbol{D} \to \mathbb{R}$ is a non-negative continuous function. Then there exists an additional feedback control v such that when $\rho(t,x)$ and κ_0 are known, the total control $u = \varphi(t,x) + v$ can achieve stability of system even in the presence of perturbations.

Definition 2 [41]. (Input-to-State Stable): Considering the system

$$\dot{x} = f(t,x,u) \tag{20}$$

where $f : [0,\infty) \times \mathbb{R}^n \times \mathbb{R}^m \to \mathbb{R}^n$ is continuous with respect to t and locally Lipschitz with respect to x and u. Input $u(t)$ is bounded for all $t \ge 0$. If there exists a KL-class function β and a K-class function γ such that for any initial time t_0, initial state x_0, and bounded input $u(t)$, the solution $x(t)$ exists for all $t \ge t_0$ and satisfies

$$\left\| x(t) \right\| \le \beta\left(\left\| x(t_0) \right\|, t - t_0 \right) + \gamma\left(\sup_{t_0 \le \tau \le t} \left\| u(\tau) \right\| \right) \tag{21}$$

then the system (20) is Input-to-State Stable(ISS).

As for the subsystem with actuator faults studied in this paper

$$\dot{\boldsymbol{x}}_2 = \boldsymbol{f}_2 + \boldsymbol{g}_2(\boldsymbol{\tau}\boldsymbol{u} + \boldsymbol{\upsilon}) \tag{22}$$

Define the key variable $\boldsymbol{w} = \boldsymbol{g}_2^{\mathrm{T}}\left[\partial V / \partial \boldsymbol{x}_2\right]^{\mathrm{T}}$, whose dynamics take the following form

$$\begin{aligned}\dot{\boldsymbol{w}} &= \frac{d}{dt}\left[\boldsymbol{g}_2^{\mathrm{T}}\left(\partial V/\partial \boldsymbol{x}_2\right)^{\mathrm{T}}\right] \\ &= \frac{\partial \boldsymbol{w}}{\partial t} + \frac{\partial \boldsymbol{w}}{\partial \boldsymbol{x}_2}\dot{\boldsymbol{x}}_2 \\ &= \frac{\partial \boldsymbol{w}}{\partial t} + \frac{\partial \boldsymbol{w}}{\partial \boldsymbol{x}_2}\bar{\boldsymbol{f}}_2 + \frac{\partial \boldsymbol{w}}{\partial \boldsymbol{x}_2}\boldsymbol{g}_2\left[\left(\boldsymbol{\tau}-\boldsymbol{I}\right)\boldsymbol{u}_n + \boldsymbol{\tau}\boldsymbol{v} + \boldsymbol{v}\right] \\ &= \frac{\partial \boldsymbol{w}}{\partial t} + \boldsymbol{L}_{\bar{f}}\boldsymbol{w} + \boldsymbol{L}_g\boldsymbol{w}\left[\left(\boldsymbol{\tau}-\boldsymbol{I}\right)\boldsymbol{u}_n + \boldsymbol{\tau}\boldsymbol{v} + \boldsymbol{v}\right]\end{aligned} \tag{23}$$

Where $\bar{\boldsymbol{f}} = \boldsymbol{f}_2 + \boldsymbol{g}_2\boldsymbol{u}_n$, $\boldsymbol{u}_n$ is the stabilizing control law for the nominal system which will be introduced in section 3.3. $\boldsymbol{L}_{\bar{f}}\boldsymbol{w} = \left(\partial \boldsymbol{w}/\partial \boldsymbol{x}_2\right)\bar{\boldsymbol{f}}_2$ and $\boldsymbol{L}_g\boldsymbol{w} = \left(\partial \boldsymbol{w}/\partial \boldsymbol{x}_2\right)\boldsymbol{g}_2$.

Assumption 2. The vector relative degree of the output $\boldsymbol{w}$ with respect to the control $\boldsymbol{v}$ is $\boldsymbol{r} = \boldsymbol{I}_m$, i.e., matrix $\boldsymbol{L}_g\boldsymbol{w}(t,x)$ is invertible. Moreover, there exist constants $0 < \bar{\alpha}_1 \le \bar{\alpha}_2$ such that $\forall(t,x)$

$$\bar{\alpha}_1 \le \left|\det\left\{\boldsymbol{L}_g\boldsymbol{w}(t,x)\right\}\right| \le \bar{\alpha}_2 \tag{24}$$

Remark 2. In classical Lyapunov redesign, system uncertainty is substantially mitigated by a robust feedback component v, driving the closed-loop system to the equilibrium achieved by the nominal control law [20][21]. This continuous convergence differs from the two-phase convergence in sliding mode control [30][31],**Error! Reference source not found.**. Nevertheless, by leveraging the Lyapunov-based robustness framework, an integrated sliding-mode and Lyapunov redesign approach is developed for enhanced uncertainty rejection, as detailed in Section 3.2.

Remark 3. Assumption 2 ensures that the control input $\boldsymbol{v}$ is explicitly decoupled from the output derivative $\dot{\boldsymbol{w}}$, meaning the output is directly influenced by the input. When the relative order is 1, the sliding surface can be directly defined as $\boldsymbol{s} = \boldsymbol{w}$ [35][36][37]. However, a linear sliding surface reduces the convergence speed near the origin and induces severe chattering once reached. Therefore, this paper proposes an improved nonlinear sliding surface that avoids the aforementioned issues.

3.2. Sliding-mode-based Lyapunov redesign

Assumption 2 enables the design of linear sliding surfaces $\boldsymbol{s} = \boldsymbol{w}$, providing a basic framework for integrating sliding mode control with Lyapunov redesign. To enhance the convergence rate near the origin while suppressing chattering, we design a novel nonlinear sliding surface. The nonlinear function $\boldsymbol{\phi}(\square)$ is chosen as $\boldsymbol{\phi}(\boldsymbol{w}) = \boldsymbol{w}e^{-\boldsymbol{w}^2}$. Which obviously satisfies $\boldsymbol{\phi}(0) = 0, \boldsymbol{w}^T\boldsymbol{\phi}(\boldsymbol{w}) > 0$ for all $\boldsymbol{w} \ne 0$ (since $e^{-\boldsymbol{w}^2} > 0$ everywhere), $\boldsymbol{\phi} \in C^1$, and $\boldsymbol{\phi}'(0) = \boldsymbol{I}$. Using this function, the nonlinear sliding surface is defined as

$$\boldsymbol{s} = \boldsymbol{w} + \boldsymbol{k}_\phi\boldsymbol{\phi}(\boldsymbol{w}) + \boldsymbol{k}_I\int_0^t \boldsymbol{w}(\tau)d\tau \tag{25}$$

where $\boldsymbol{k}_\phi = diag(k_{\phi 1}, k_{\phi 2}, k_{\phi 3})$ and $\boldsymbol{k}_I = diag(k_{I_1}, k_{I_2}, k_{I_3})$ are positive definite parameter matrices. This diagonal structure guarantees commutativity with vector operations, which will be used in the subsequent Lyapunov analysis.

Considering the nonlinear function

$$\begin{cases}\boldsymbol{\phi}(\boldsymbol{w}) = \boldsymbol{w}e^{-\boldsymbol{w}^2},\ \boldsymbol{\phi}(0) = 0 \\ \boldsymbol{w}^T\boldsymbol{\phi}(\boldsymbol{w}) > 0 \quad \textit{for all } \boldsymbol{w} \ne 0 \\ \boldsymbol{\phi}'(\boldsymbol{w}) = e^{-\boldsymbol{w}^2}\left(1 - 2\boldsymbol{w}^2\right)\end{cases} \tag{26}$$

Compared with conventional linear surfaces $\boldsymbol{s} = \boldsymbol{w}$. The proposed sliding surface provides high gain near the origin where strong robustness is needed, and low gain in large-deviation regions where actuator protection is desired, all in a fully smooth manner. While we cannot claim that this particular functional form is "optimal" among all possible nonlinear functions, it achieves a more balanced design trade-off among convergence speed, singularity avoidance, and signal smoothness compared with linear and conventional terminal sliding surfaces [42].

Therefore, the proposed sliding surface guarantees the continuous differentiability of control law over the entire

state space including the origin, providing a theoretical basis for generating smooth control signals. The continuous total control law $\boldsymbol{u}$ is designed as follow

$$\begin{aligned}\boldsymbol{u} &= \boldsymbol{u}_n + \boldsymbol{v}\\ \boldsymbol{v} &= -\left(\boldsymbol{M}(\boldsymbol{w})\right)^{-1}\left(\boldsymbol{k}_1\boldsymbol{\Xi}_1(\boldsymbol{s}) + \boldsymbol{z}_n + \boldsymbol{\mu}_1\boldsymbol{s}\right)\\ \dot{\boldsymbol{z}}_n &= -\boldsymbol{k}_2\boldsymbol{\Xi}_2(\boldsymbol{s}) - \boldsymbol{\mu}_2\boldsymbol{z}_n\end{aligned} \tag{27}$$

where $\boldsymbol{u}_n$ is the nominal control law and $\boldsymbol{v}$ is the compensation control law, $\boldsymbol{M}(\boldsymbol{w}) = \left[\boldsymbol{I} + \boldsymbol{k}_\phi\phi'(\boldsymbol{w})\right]\boldsymbol{L}_g\boldsymbol{w}$ is the gain control matrix. $\boldsymbol{k}_1, \boldsymbol{k}_2$ are positive definite parameter matrices. $\boldsymbol{\mu}_1, \boldsymbol{\mu}_2$ are small constant matrices to enhance stability near the origin. $\boldsymbol{z}_n$ is an auxiliary variable. $\boldsymbol{\Xi}_1(\boldsymbol{s}), \boldsymbol{\Xi}_2(\boldsymbol{s})$ are smoothing functions used to ensure the continuity of control inputs.

$$\begin{aligned}\boldsymbol{\Xi}_1(\boldsymbol{s}) &= \left(\boldsymbol{1} + |\boldsymbol{s}|^\alpha\right) \circ \tanh\left(\frac{\boldsymbol{s}}{\boldsymbol{\varepsilon}}\right), \alpha \in (0,1)\\ \boldsymbol{\Xi}_2(\boldsymbol{s}) &= \left(\boldsymbol{1} + |\boldsymbol{s}|^\beta\right) \circ \tanh\left(\frac{\boldsymbol{s}}{\boldsymbol{\varepsilon}}\right), \beta = \frac{2\alpha}{1+\alpha}\end{aligned} \tag{28}$$

Where operator $\circ$ represents the Hadamard product, $\boldsymbol{1}$ is the all-ones vector, $|\boldsymbol{s}|^\alpha$ denotes the elementwise $|s_i|^\alpha$, and $\tanh(\square)$ acts elementwise, $\boldsymbol{\varepsilon}$ is a positive parameter to be selected. While higher-order sliding-mode algorithms can generate continuous control without explicit smoothing, they typically require more stringent gain tuning and may respond more slowly to abrupt faults. The proposed boundary-layer approach preserves the Lyapunov redesign framework, ensures $\boldsymbol{C}^1$ continuity of $\boldsymbol{v}$, and suppresses chattering without compromising the finite-time convergence guaranteed by Theorem 1.

Since the designed sliding mode surface $\boldsymbol{s}$ is an explicit function of $\boldsymbol{w}$. Considering Assumption 2 and the function $\phi(\square)$, the following lemma can be derived.

Lemma 1. Suppose the nonlinear term satisfies $\det\left\{\boldsymbol{I} + \boldsymbol{k}_\phi\phi'(\boldsymbol{w})\right\} \neq 0$ for all $\boldsymbol{w} \neq 0$. Then the sliding surface (25) also has vector relative degree $\boldsymbol{r} = \boldsymbol{I}_m$ with respect to $\boldsymbol{v}$, and the control gain matrix $\boldsymbol{M}(\boldsymbol{w}) = \left[\boldsymbol{I} + \boldsymbol{k}_\phi\phi'(\boldsymbol{w})\right]\boldsymbol{L}_g\boldsymbol{w}$ is invertible. Furthermore, if there exist constants $0 < \bar{\gamma}_1 \le \bar{\gamma}_2$ such that $\bar{\gamma}_1 \le \left|\det\left\{\boldsymbol{L}_g\boldsymbol{w}(t,x)\right\}\right| \le \bar{\gamma}_2$ (Assumption 2) and $\boldsymbol{I} + \boldsymbol{k}_\phi\phi'(\boldsymbol{w})$ is bounded, then there exist constants $0 < \bar{\alpha}_3 \le \bar{\alpha}_4$ such that $\forall \boldsymbol{w}$

$$\bar{\alpha}_3 \le \left|\det\left\{\boldsymbol{M}(\boldsymbol{w})\right\}\right| \le \bar{\alpha}_4 \tag{29}$$

Proof. The proof of Lemma 1 is devided into two steps. Firstly, verify the vector relative degree of $\boldsymbol{s}$ with respect to the control is $\boldsymbol{r} = \boldsymbol{I}_m$ and $\boldsymbol{M}(\boldsymbol{w})$ is invertible.Then verify the boundedness of $\boldsymbol{M}(\boldsymbol{w})$.

Step 1: Differentiating the sliding surface (25) yields

$$\dot{\boldsymbol{s}} = \dot{\boldsymbol{w}} + \boldsymbol{k}_\phi\phi'(\boldsymbol{w})\dot{\boldsymbol{w}} + \boldsymbol{k}_I\dot{\boldsymbol{w}} = \left[\boldsymbol{I} + \boldsymbol{k}_\phi\phi'(\boldsymbol{w})\right]\dot{\boldsymbol{w}} + \boldsymbol{k}_I\boldsymbol{w} \tag{30}$$

Since the vector relative degree of the output $\boldsymbol{w}$ with respect to the control $\boldsymbol{v}$ is $\boldsymbol{r} = \boldsymbol{I}_m$, then the dynamics of $\boldsymbol{w}$ can be described as $\dot{\boldsymbol{w}} = \boldsymbol{a}(\boldsymbol{w}) + \boldsymbol{b}(\boldsymbol{w})\boldsymbol{v}$, where $\boldsymbol{b}(\boldsymbol{w}) = \boldsymbol{L}_g\boldsymbol{w}$ is invertible. Thus

$$\begin{aligned}\dot{\boldsymbol{s}} &= \left[\boldsymbol{I} + \boldsymbol{k}_\phi\phi'(\boldsymbol{w})\right]\left[\boldsymbol{a}(\boldsymbol{w}) + \boldsymbol{b}(\boldsymbol{w})\boldsymbol{v}\right] + \boldsymbol{k}_I\boldsymbol{w}\\ &= \left[\boldsymbol{I} + \boldsymbol{k}_\phi\phi'(\boldsymbol{w})\right]\boldsymbol{a}(\boldsymbol{w}) + \boldsymbol{k}_I\boldsymbol{w} + \left[\boldsymbol{I} + \boldsymbol{k}_\phi\phi'(\boldsymbol{w})\right]\boldsymbol{L}_g\boldsymbol{w}\boldsymbol{v}\end{aligned} \tag{31}$$

Eq. (31) indicates that $\dot{\boldsymbol{s}}$ explicitly depends on $\boldsymbol{v}$, with the coefficient matrix $\boldsymbol{M}(\boldsymbol{w})$. As for designed $\phi'(\boldsymbol{w})$ in this paper, $|\phi'(\boldsymbol{w})| \le 1$ holds for all $\boldsymbol{w}$. Thus for $0 < k_{\phi i} < 1, i = 1,2,3$, $1 + k_{\phi i}\phi'(w_i) \ge 1 - k_{\phi i} > 0$ holds. This means that $\boldsymbol{I} + \boldsymbol{k}_\phi\phi'(\boldsymbol{w})$ is invertible.

Thus, $\boldsymbol{M}(\boldsymbol{w})$ is invertible and the vector relative degree of $\boldsymbol{s}$ with respect to the control is $\boldsymbol{r} = \boldsymbol{I}_m$.

Step 2: The determinant satisfies

$$\left|\det\left\{\boldsymbol{M}(\boldsymbol{w})\right\}\right| = \left|\det\left\{\left[\boldsymbol{I} + \boldsymbol{k}_\phi\phi'(\boldsymbol{w})\right]\boldsymbol{L}_g\boldsymbol{w}\right\}\right| = \left|\det\left\{\boldsymbol{I} + \boldsymbol{k}_\phi\phi'(\boldsymbol{w})\right\}\right| \cdot \left|\det\left\{\boldsymbol{L}_g\boldsymbol{w}\right\}\right| \tag{32}$$

Since $\boldsymbol{I} + \boldsymbol{k}_\phi\phi'(\boldsymbol{w})$ is diagonal, thus

$$\left|\det\left\{\boldsymbol{I}+\boldsymbol{k}_{\phi}\phi'(\boldsymbol{w})\right\}\right|=\prod_{i=1}^{m}\left|1+k_{\phi i}\phi'(w_i)\right|=\prod_{i=1}^{m}1+k_{\phi i}\phi'(w_i),\ \ as\ 1+k_{\phi i}\phi'(w_i)>0 \tag{33}$$

From $\left|\phi'(\boldsymbol{w})\right|\le 1$ and $0<k_{\phi i}<1, i=1,2,3$

$$1-k_{\phi i}\le 1+k_{\phi i}\phi'(w_i)\le 1+k_{\phi i} \tag{34}$$

Thus

$$\prod_{i=1}^{m}\left(1-k_{\phi i}\right)\le\left|\det\left\{\boldsymbol{I}+\boldsymbol{k}_{\phi}\phi'(\boldsymbol{w})\right\}\right|\le\prod_{i=1}^{m}\left(1+k_{\phi i}\right) \tag{35}$$

Let $\underline{\beta}_1=\prod_{i=1}^{m}\left(1-k_{\phi i}\right)>0$ and $\underline{\beta}_2=\prod_{i=1}^{m}\left(1+k_{\phi i}\right)<\infty$, yielding

$$\underline{\beta}_1\le\left|\det\left\{\boldsymbol{I}+\boldsymbol{k}_{\phi}\phi'(\boldsymbol{w})\right\}\right|\le\underline{\beta}_2 \tag{36}$$

From the original assumption: $\bar{\gamma}_1\le\left|\det\left\{\boldsymbol{L}_{\boldsymbol{g}}\boldsymbol{w}(t,x)\right\}\right|\le\bar{\gamma}_2$. Substituting into (32)

$$\bar{\gamma}_1\underline{\beta}_1\le\det\left\{\boldsymbol{M}(\boldsymbol{w})\right\}\le\bar{\gamma}_2\underline{\beta}_2 \tag{37}$$

Setting $\bar{\alpha}_3=\bar{\gamma}_1\underline{\beta}_1>0$ and $\bar{\alpha}_4=\bar{\gamma}_2\underline{\beta}_2<\infty$ satisfies $\bar{\alpha}_3\le\left|\det\left\{\boldsymbol{M}(\boldsymbol{w})\right\}\right|\le\bar{\alpha}_4$, which means $\boldsymbol{M}(\boldsymbol{w})$ is bounded

The proof of Lemma 1 is complete.

Lemma 2 [43]. Suppose that there exists a continuous and positive Lyapunov function V, and that

$$\dot{V}(x)+cV(x)^{\alpha}\le 0, x\in U\setminus 0 \tag{38}$$

Where U denotes an open neighborhood of the origin of a controlled system, $x\in\mathbb{R}^n, c>0, \alpha\in(0,1)$. Thus, the system state converges to the equilibrium point in finite-time, and the convergence time T satisfies

$$T\le\frac{1}{c(1-\alpha)}V(x(0))^{1-\alpha} \tag{39}$$

Assumption 3. There exist constants L_{ω} and δ_{ω} such that

$$\begin{aligned}\left\|\left(\boldsymbol{I}+\boldsymbol{k}_{\phi}\phi'(\boldsymbol{w})\right)\left(\frac{\partial\boldsymbol{w}}{\partial t}+\boldsymbol{L}_{\bar{\boldsymbol{f}}}\boldsymbol{w}\right)\right\|&\le L_{\omega}\\ \left\|\boldsymbol{M}(\boldsymbol{w})\left[(\boldsymbol{\tau}-\boldsymbol{I})\boldsymbol{u}_{\boldsymbol{n}}+\boldsymbol{v}\right]\right\|&\le\delta_{\omega}\end{aligned} \tag{40}$$

Remark 4. In the nonlinear sliding surface Eq. (25), both gain matrices are chosen to be positive-definite diagonal matrices. This diagonal structure ensures commutativity with vector operations in the subsequent Lyapunov derivations. $\boldsymbol{k}_{\phi}$ adjusts the influence of the nonlinear terms, helping to shape the sliding surface dynamics near the origin. While $\boldsymbol{k}_{\boldsymbol{I}}$ provides integral action to suppress steady-state errors in the key variable $\boldsymbol{w}$. Furthermore, the sliding surface design combined with the control variable $\boldsymbol{v}$ ensures that the control law is continuously differentiable at $\boldsymbol{s}\to 0$.

Remark 5. Unlike the super-twisting algorithm or the fractional-power smoothing function, the proposed modified function (28) offers superior chattering suppression. The $\tanh(\cdot)$ function is infinitely differentiable, ensuring that the control input v is globally continuous and Lipschitz. Furthermore, because the fractional power term $|\boldsymbol{s}|^{\alpha}$ is multiplied by the saturated $\tanh$ term, the control signal does not experience abrupt switching even when $\boldsymbol{s}$ crosses zero. This property is highly beneficial for preserving the service life of physical actuators on morphing aircraft.

Remark 6. As for Assumption 3. According to Assumption 1 and Lemma 1, it is easily derived that $\left\|\boldsymbol{M}(\boldsymbol{w})\right\|$, $\left\|\boldsymbol{\tau}-\boldsymbol{I}\right\|$ and $\left\|\boldsymbol{I}+\boldsymbol{k}_{\phi}\phi'(\boldsymbol{w})\right\|$ are bounded. The assumption of boundedness for the remaining terms is also common [27],[28],[29]. This assumption forms the basis for subsequent stability analysis.

3.3. SMLR based fault-tolerant controller design

The sliding-mode Lyapunov redesign based fault-tolerant controller is designed to suppress the uncertainty caused by actuator faults in the system (10). The controller design will be carried out in two steps.

Step 1: (Nominal Controller Design via Backstepping Control) For the nominal system with $\tau_i = 1$ and $\upsilon_i = 0$, design $\boldsymbol{u}_n$ via backstepping control method such that asymptotic stability of the origin of the nominal system is ensured. Besides, this ensures the boundedness of both $\boldsymbol{x}(t)$ and $\boldsymbol{u}_n(t)$.

Step 2: (Fault-Tolerant Control via Sliding-Mode Lyapunov Redesign) Leveraging Assumption 1 and the boundedness of $\boldsymbol{u}_n(t)$. The fault-tolerant control problem is defined as follows: Construct the sliding surface (25) and design a compensation term (27) for actuator faults such that the closed-loop system (10) achieves ultimate boundedness.

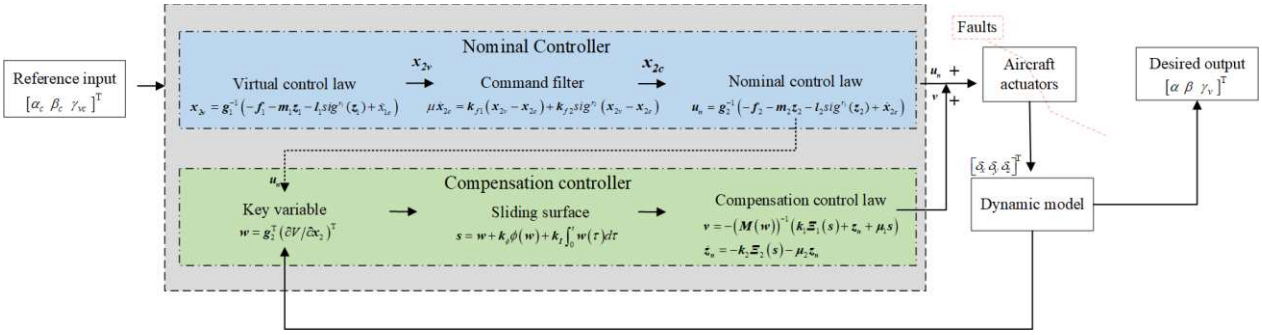


Fig. 1 System diagram of the proposed control scheme

To provide a clearer visual of the overall framework of the proposed control scheme, Fig. 1 presents a complete block diagram. This diagram connects the nominal controller design with the fault-tolerant compensation design.

Firstly, the nominal system with $\tau_i = 1$ and $\upsilon_i = 0$ is as follow

$$\begin{cases} \dot{\boldsymbol{x}}_1 = \boldsymbol{f}_1 + \boldsymbol{g}_1 \boldsymbol{x}_2 \\ \dot{\boldsymbol{x}}_2 = \boldsymbol{f}_2 + \boldsymbol{g}_2 \boldsymbol{u} \end{cases} \tag{41}$$

For the reference command $\boldsymbol{x}_{1c} = \left[\alpha_c \quad \beta_c \quad \gamma_{Vc}\right]^{\mathrm{T}}$. The system error of attitude angles are represented by

$$\boldsymbol{z}_1 = \boldsymbol{x}_1 - \boldsymbol{x}_{1c} \tag{42}$$

By combining the dynamic surface backstepping method with Lemma 2. The following virtual control low is designed to achieve the finite time stability

$$\boldsymbol{x}_{2v} = \boldsymbol{g}_1^{-1}\left(-\boldsymbol{f}_1 - \boldsymbol{m}_1 \boldsymbol{z}_1 - \boldsymbol{l}_1 sig^{r_1}(\boldsymbol{z}_1) + \dot{\boldsymbol{x}}_{1c}\right) \tag{43}$$

where $\boldsymbol{m}_1, \boldsymbol{l}_1$ are positive define parameter matrices and $sig^r(x) = |x|^r sign(x)$. $0 < r_1 \le 1$ is designed parameter. To avoid possible differential explosion problems, the virtual control command $\boldsymbol{x}_{2v}$ is passed through a first-order finite time command filter to get the filtered angle rate command $\boldsymbol{x}_{2c}$.

$$\begin{aligned} &\mu_f \dot{\boldsymbol{x}}_{2c} = \boldsymbol{k}_{f1}\left(\boldsymbol{x}_{2v} - \boldsymbol{x}_{2c}\right) + \boldsymbol{k}_{f2} sig^{r_2}\left(\boldsymbol{x}_{2v} - \boldsymbol{x}_{2c}\right) \\ &\boldsymbol{x}_{2c}(0) = \boldsymbol{x}_{2v}(0) \end{aligned} \tag{44}$$

where $\boldsymbol{k}_{f1}, \boldsymbol{k}_{f2}$ are positive define parameter matrices respectively, r_2 is designed parameter, $\mu_f > 0$ is the filter parameter. In the nominal backstepping procedure, the derivative $\dot{\boldsymbol{x}}_{2v}$ would be needed analytically, which leads to the "explosion of terms" and requires unjustified a priori boundedness claims. In contrast, the dynamic surface control (DSC) framework [44] avoids this difficulty by introducing a first-order filter and by constructing an explicit compact set on which all signals, including the filter output and its derivative, are guaranteed to be bounded without assuming stability a priori. The subsequent proof adopts this strategy: the filter state $\boldsymbol{z}_f$ is included in the Lyapunov function V_n with a weighting factor $\mu_f > 0$ that scales the effective filter bandwidth. The filter dynamics are used to characterize the boundedness of $\dot{\boldsymbol{x}}_{2c}$ (and consequently $\dot{\boldsymbol{x}}_{2v}$) on the achievable compact set.

Similarly, error of angle rates are represented by $\boldsymbol{z}_2 = \boldsymbol{x}_2 - \boldsymbol{x}_{2c}$. A nominal control law of the following form can be designed

$$\boldsymbol{u}_n = \boldsymbol{g}_2^{-1}\left(-\boldsymbol{f}_2 - \boldsymbol{m}_2 \boldsymbol{z}_2 - \boldsymbol{l}_2 sig^{r_3}(\boldsymbol{z}_2) + \dot{\boldsymbol{x}}_{2c}\right) \tag{45}$$

Then the main result of nominal controller design is given by the following theorem.

Theorem 1: Considering the nominal system (41), the virtual control law (43) and the nominal control law (45), if the parameters are properly selected, then the finite-time stability of nominal system is ensured. The system error converges to a bounded neighborhood near the origin in finite time, and further the control input is bounded.

Proof. Define the error of finite time command filter as $z_f = x_{2v} - x_{2c}$

$$\dot{z}_f = \dot{x}_{2v} - \mu_f^{-1}\left(k_{f1} z_f + k_{f2} sig^{r_2}\left(z_f\right)\right) \tag{46}$$

The Lyapunov function for the nominal system is selected as

$$\begin{aligned} V_n &= V_{n1} + V_{n2} + V_{nf} \\ &= \frac{1}{2} z_1^{\mathrm{T}} m_1^{-1} z_1 + \frac{1}{2} z_2^{\mathrm{T}} m_2^{-1} z_2 + \frac{\mu_f}{2} z_f^{\mathrm{T}} z_f \end{aligned} \tag{47}$$

The derivative is calculated as

$$\begin{aligned} \dot{V}_n &= z_1^{\mathrm{T}} m_1^{-1} \dot{z}_1 + z_2^{\mathrm{T}} m_2^{-1} \dot{z}_2 + \mu_f z_f^{\mathrm{T}} \dot{z}_f \\ &= z_1^{\mathrm{T}} m_1^{-1}\left(-m_1 z_1 - l_1 sig^{r_1}(z_1)\right) + z_2^{\mathrm{T}} m_2^{-1}\left(-m_2 z_2 - l_2 sig^{r_3}(z_2)\right) \\ &\quad + \mu_f z_f^{\mathrm{T}}\left[\dot{x}_{2v} - \mu_f^{-1}\left(k_{f1} z_f + k_{f2} sig^{r_2}\left(z_f\right)\right)\right] \end{aligned} \tag{48}$$

Expand and format as follows

$$\begin{aligned} \dot{V}_n &= -z_1^{\mathrm{T}} z_1 - z_1^{\mathrm{T}} m_1^{-1} l_1 sig^{r_1}(z_1) - z_2^{\mathrm{T}} z_2 - z_2^{\mathrm{T}} m_2^{-1} l_2 sig^{r_3}(z_2) \\ &\quad + \mu_f z_f^{\mathrm{T}} \dot{x}_{2v} - z_f^{\mathrm{T}}\left(k_{f1} z_f + k_{f2} sig^{r_2}\left(z_f\right)\right) \end{aligned} \tag{49}$$

To Handle the virtual control derivative via explicit compact set argument. Considering the output of the finite-time command filter x_{2c} and the filter error z_2, from which we obtain $x_2 = z_2 + x_{2c} = z_2 + x_{2v} - z_f$. The virtual control x_{2v} is a smooth function of z_1 and the reference signals. Therefore it is continuous on any neighborhood of the origin. In the derivative of V_n, the cross-term involving $\dot{x}_{2v}$ appears as $\mu_f z_f^{\mathrm{T}} \dot{x}_{2v}$. We rewrite it as

$$\mu_f z_f^{\mathrm{T}} \dot{x}_{2v} = \mu_f z_f^{\mathrm{T}} \dot{x}_{2c} + \mu_f z_f^{\mathrm{T}} \dot{z}_f \tag{50}$$

From the filter dynamics, the finite-time convergence of the filter ensures that $\|z_f\|$ and $\|\dot{z}_f\|$ converge to a small neighborhood of zero in finite time. Consequently, there exist positive constants β_a, β_b (determined solely by the filter gains, μ_f and the reference bounds) such that $\|\dot{z}_f\| \le \beta_a, \|\dot{x}_{2c}\| \le \beta_b$ in a finite time. Let $\beta = \max\{\beta_a, \beta_b\}$ Therefore

$$\left\|\mu_f z_f^{\mathrm{T}} \dot{x}_{2v}\right\| \le \mu_f \|z_f\|\left(\|\dot{x}_{2c}\| + \|z_f\|\right) \le 2\mu_f \beta \|z_f\| \tag{51}$$

Applying Young's inequality

$$\mu_f z_f^{\mathrm{T}} \dot{x}_{2v} \le \left|\mu_f z_f^{\mathrm{T}} \dot{x}_{2v}\right| \le \frac{1}{2}\|z_f\|^2 + 2\mu_f^2 \beta^2 \tag{52}$$

The bound is completely expressed in terms of the filter error z_f and the known constants β, μ_f without unknown constant.

For the quadratic and nonlinear terms

$$\begin{aligned} z_1^{\mathrm{T}} z_1 &\ge \lambda_{\min}\left(m_1\right) \cdot z_1^{\mathrm{T}} m_1^{-1} z_1 = 2\lambda_{\min}\left(m_1\right) V_{n1} \\ z_2^{\mathrm{T}} z_2 &\ge \lambda_{\min}\left(m_2\right) \cdot z_2^{\mathrm{T}} m_2^{-1} z_2 = 2\lambda_{\min}\left(m_2\right) V_{n2} \\ z_f^{\mathrm{T}} z_f &\ge \frac{2}{\mu_f} V_{nf} \end{aligned} \tag{53}$$

$$\begin{aligned} -z_1^{\mathrm{T}} m_1^{-1} l_1 sig^{r_1}(z_1) &\le -\frac{\lambda_{\min}\left(l_1\right)}{\lambda_{\max}\left(m_1\right)}\|z_1\|^{r_1+1} \\ -z_2^{\mathrm{T}} m_2^{-1} l_2 sig^{r_3}(z_2) &\le -\frac{\lambda_{\min}\left(l_2\right)}{\lambda_{\max}\left(m_2\right)}\|z_2\|^{r_3+1} \\ -z_f^{\mathrm{T}} k_{f2} sig^{r_2}\left(z_f\right) &\le -\lambda_{\min}\left(k_{f2}\right)\|z_f\|^{r_2+1} \end{aligned} \tag{54}$$

Substituting Eq.(52) (53) and (54) into (49) yields

$$\begin{aligned}\dot{V}_n \le & -\boldsymbol{z}_1^{\mathrm{T}}\boldsymbol{z}_1 - \frac{\lambda_{\min}\left(\boldsymbol{l}_1\right)}{\lambda_{\max}\left(\boldsymbol{m}_1\right)}\left\|\boldsymbol{z}_1\right\|^{r_1+1} - \boldsymbol{z}_2^{\mathrm{T}}\boldsymbol{z}_2 - \frac{\lambda_{\min}\left(\boldsymbol{l}_2\right)}{\lambda_{\max}\left(\boldsymbol{m}_2\right)}\left\|\boldsymbol{z}_2\right\|^{r_3+1} \\ & -c_3\left\|\boldsymbol{z}_f\right\|^2 - \lambda_{\min}\left(\boldsymbol{k}_{f2}\right)\left\|\boldsymbol{z}_f\right\|^{r_2+1} + 2\mu_f^2\beta^2\end{aligned} \tag{55}$$

Choosing $\boldsymbol{k}_{f1}$ such that $\lambda_{\min}\left(\boldsymbol{k}_{f1}\right) > 1/2$, where $c_3 = \lambda_{\min}\left(\boldsymbol{k}_{f1} - \boldsymbol{I}/2\right) > 0$. Similar with Eq. (53), the following inequality holds

$$\begin{aligned}\left\|\boldsymbol{z}_1\right\|^{r_1+1} &= \left(\left\|\boldsymbol{z}_1\right\|^2\right)^{\frac{r_1+1}{2}} \ge \left(2\lambda_{\min}\left(\boldsymbol{m}_1\right)V_{n1}\right)^{\frac{r_1+1}{2}} \\ \left\|\boldsymbol{z}_2\right\|^{r_3+1} &\ge \left(2\lambda_{\min}\left(\boldsymbol{m}_2\right)V_{n2}\right)^{\frac{r_3+1}{2}} \\ \left\|\boldsymbol{z}_f\right\|^{r_2+1} &\ge \left(\frac{2}{\mu_f}V_{nf}\right)^{\frac{r_2+1}{2}}\end{aligned} \tag{56}$$

Substituting Eq. (56) into Eq. (55) yields

$$\dot{V}_n \le -cV_n - \kappa_1\left(2\lambda_{\min}\left(\boldsymbol{m}_1\right)V_{n1}\right)^{\frac{r_1+1}{2}} - \kappa_2\left(2\lambda_{\min}\left(\boldsymbol{m}_2\right)V_{n2}\right)^{\frac{r_3+1}{2}} - \kappa_f\left(\frac{2}{\mu_f}V_{nf}\right)^{\frac{r_2+1}{2}} + D \tag{57}$$

Where $c = \min\left\{2\lambda_{\min}\left(\boldsymbol{m}_1\right), 2\lambda_{\min}\left(\boldsymbol{m}_2\right), 2c_3/\mu_f\right\}$. In this design, we set $r_1 = r_2 = r_3 = 0.5, \gamma = \left(r+1\right)/2$. Consequently, the nonlinear terms in (57) are all of the form $-\kappa_i V_{ni}^{\gamma}, i = 1, 2, f$. For $0 < \gamma < 1$ and any non-negative numbers a, b, c satisfy $a^{\gamma} + b^{\gamma} + c^{\gamma} \ge \left(a+b+c\right)^{\gamma}$, which yields

$$-\sum_{i=1}^{3}\kappa_i V_{ni}^{\gamma} \le -\left(\min_i \kappa_i\right)\left(V_{n1} + V_{n2} + V_{nf}\right)^{\gamma} = -kV_n^{\gamma} \tag{58}$$

With this, together with the quadratic bounds, we obtain the compact form

$$\dot{V}_n \le -cV_n - kV_n^{\gamma} + D \tag{59}$$

Thus V_n converges to the compact set $\left\{V_n\left(t\right) \le \left(D/k\right)^{1/r}\right\}$ in $T = \left(V_n^{1-r}\left(0\right) - \delta^{1-r}\right)\Big/\left(k\left(1-r\right)\right), \delta = \left(D/k\right)^{1/r}$. Inside the compact set, all states are bounded, and by continuity $\left\|\dot{\boldsymbol{x}}_{2v}\right\|$ is uniformly bounded.

The filter parameters k_{f1}, k_{f2}, μ_f are selected together with the surface gains to ensure c is large enough to dominate the linear perturbation. This is always possible because μ_f can be chosen small to reduce the effective perturbation, or the gains can be increased.

This concludes the proof.

After achieving finite-time convergence of the nominal control system. Based on proposed sliding mode surface (25) and robust control law (27). The detailed dynamics of the sliding mode surface is as follows

$$\begin{aligned}\dot{\boldsymbol{s}} &= \dot{\boldsymbol{w}} + \boldsymbol{k}_{\phi}\phi'\left(\boldsymbol{w}\right)\dot{\boldsymbol{w}} + \boldsymbol{k}_{\boldsymbol{I}}\boldsymbol{w} \\ &= \left[\boldsymbol{I} + \boldsymbol{k}_{\phi}\phi'\left(\boldsymbol{w}\right)\right]\left\{\frac{\partial \boldsymbol{w}}{\partial t} + \boldsymbol{L}_{\bar{\boldsymbol{f}}}\boldsymbol{w} + \boldsymbol{L}_{\boldsymbol{g}}\boldsymbol{w}\left[\left(\boldsymbol{\tau} - \boldsymbol{I}\right)\boldsymbol{u}_{\boldsymbol{n}} + \boldsymbol{\tau}\boldsymbol{v} + \boldsymbol{v}\right]\right\} + \boldsymbol{k}_{\boldsymbol{I}}\boldsymbol{w} \\ &= -\boldsymbol{\tau}\left(\boldsymbol{k}_1\boldsymbol{\Xi}_1\left(\boldsymbol{s}\right) + \boldsymbol{z}_{\boldsymbol{n}} + \boldsymbol{\mu}_1\boldsymbol{s}\right) + \left(\boldsymbol{I} + \boldsymbol{k}_{\phi}\phi'\left(\boldsymbol{w}\right)\right)\left(\frac{\partial \boldsymbol{w}}{\partial t} + \boldsymbol{L}_{\bar{\boldsymbol{f}}}\boldsymbol{w}\right) \\ &\quad + \boldsymbol{M}\left(\boldsymbol{w}\right)\left[\left(\boldsymbol{\tau} - \boldsymbol{I}\right)\boldsymbol{u}_{\boldsymbol{n}} + \boldsymbol{v}\right] + \boldsymbol{k}_{\boldsymbol{I}}\boldsymbol{w}\end{aligned} \tag{60}$$

Then the main result of fault-tolerant controller design is given by the following theorem.

Theorem 2: Considering the nonlinear system (22) with actuator faults. Define $\boldsymbol{w} = \boldsymbol{g}_2^{\mathrm{T}}\left[\partial V/\partial \boldsymbol{x}_2\right]^{\mathrm{T}}$. Designing the nonlinear sliding surface (25) and total control law (27). Assumption 1 and 3 are satisfied. If there exist constants $a, b > 0$ and positive definite matrices $\boldsymbol{k}_1, \boldsymbol{k}_2, \boldsymbol{\mu}_1, \boldsymbol{\mu}_2$ such that

$$\frac{1}{a}+\frac{\lambda_{\max}\left(\boldsymbol{k}_I^2\right)}{b}<2,\quad \tau_\omega\lambda_{\min}\left(\boldsymbol{\mu}_1\right)\geq\frac{a+b+1}{2}$$
$$\lambda_{\min}\left(\boldsymbol{k}_2^{-1}\boldsymbol{\mu}_2\right)>\frac{(2+m+2\sqrt{m})}{2},\quad \tau_\omega\lambda_{\min}\left(\boldsymbol{k}_1\right)\geq L_\omega+\delta_\omega \tag{61}$$

Then the closed loop system is Input-to-State Stable ((ISS)). The sliding variable $\boldsymbol{s}$ converges to the set Ω and consequently the original states $\boldsymbol{x}_1$ and $\boldsymbol{x}_2$ converge to a neighborhood of the origin.

Proof. The Lyapunov function is constructed as

$$V_s=\frac{1}{2}\boldsymbol{s}^{\mathrm{T}}\boldsymbol{s}+\frac{1}{2}\boldsymbol{z}_n^{\boldsymbol{T}}\boldsymbol{k}_2^{-1}\boldsymbol{z}_n+\frac{1}{2}\boldsymbol{e}^{\mathrm{T}}\boldsymbol{k}_I\boldsymbol{e}$$
$$\dot{V}_s=\boldsymbol{s}^{\mathrm{T}}\dot{\boldsymbol{s}}+\boldsymbol{z}_n^{\boldsymbol{T}}\boldsymbol{k}_2^{-1}\dot{\boldsymbol{z}}_n+\boldsymbol{e}^{\mathrm{T}}\boldsymbol{k}_I\dot{\boldsymbol{e}} \tag{62}$$

where $\boldsymbol{e}=\int_0^t\boldsymbol{w}(\tau)d\tau,\dot{\boldsymbol{e}}=\boldsymbol{w}$, substituting Eq. (60) and (27) into Eq. (62) yields

$$\begin{aligned}\dot{V}_s&=\boldsymbol{s}^{\mathrm{T}}\dot{\boldsymbol{s}}+\boldsymbol{z}_n^{\boldsymbol{T}}\boldsymbol{k}_2^{-1}\dot{\boldsymbol{z}}_n+\boldsymbol{e}^{\mathrm{T}}\boldsymbol{k}_I\dot{\boldsymbol{e}}\\&=\boldsymbol{s}^{\mathrm{T}}\left(\dot{\boldsymbol{w}}+\boldsymbol{k}_\phi\phi'(\boldsymbol{w})\dot{\boldsymbol{w}}+\boldsymbol{k}_I\boldsymbol{w}\right)+\boldsymbol{z}_n^{\boldsymbol{T}}\boldsymbol{k}_2^{-1}\left(-\boldsymbol{k}_2\boldsymbol{\Xi}_2(\boldsymbol{s})-\boldsymbol{\mu}_1\boldsymbol{z}_n\right)+\boldsymbol{e}^{\mathrm{T}}\boldsymbol{k}_I\boldsymbol{w}\\&=\boldsymbol{s}^{\mathrm{T}}\left\{\left(\boldsymbol{I}+\boldsymbol{k}_\phi\phi'(\boldsymbol{w})\right)\left(\frac{\partial\boldsymbol{w}}{\partial t}+\boldsymbol{L}_{\bar{f}}\boldsymbol{w}\right)+\boldsymbol{M}(\boldsymbol{w})\left[(\boldsymbol{\tau}-\boldsymbol{I})\boldsymbol{u}_n+\boldsymbol{v}\right]+\boldsymbol{k}_I\boldsymbol{w}\right\}\\&\quad-\boldsymbol{s}^{\mathrm{T}}\boldsymbol{\tau}\boldsymbol{k}_1\boldsymbol{\Xi}_1(\boldsymbol{s})-\boldsymbol{s}^{\mathrm{T}}\boldsymbol{\tau}\boldsymbol{z}_n-\boldsymbol{s}^{\mathrm{T}}\boldsymbol{\tau}\boldsymbol{\mu}_1\boldsymbol{s}-\boldsymbol{z}_n^{\boldsymbol{T}}\boldsymbol{\Xi}_2(\boldsymbol{s})-\boldsymbol{z}_n^{\boldsymbol{T}}\boldsymbol{k}_2^{-1}\boldsymbol{\mu}_2\boldsymbol{z}_n+\boldsymbol{e}^{\mathrm{T}}\boldsymbol{k}_I\boldsymbol{w}\end{aligned} \tag{63}$$

As for $\boldsymbol{s}=\boldsymbol{w}+\boldsymbol{k}_\phi\boldsymbol{\phi}(\boldsymbol{w})+\boldsymbol{k}_I\boldsymbol{e}$, thus $\boldsymbol{e}^{\mathrm{T}}\boldsymbol{k}_I\boldsymbol{w}=\boldsymbol{s}^{\mathrm{T}}\boldsymbol{w}-\boldsymbol{w}^{\mathrm{T}}\boldsymbol{w}-\boldsymbol{\phi}(\boldsymbol{w})^{\mathrm{T}}\boldsymbol{k}_\phi\boldsymbol{w}$, hence (63)

$$\begin{aligned}\dot{V}_s&=\boldsymbol{s}^{\mathrm{T}}\left(\boldsymbol{I}+\boldsymbol{k}_\phi\phi'(\boldsymbol{w})\right)\left(\frac{\partial\boldsymbol{w}}{\partial t}+\boldsymbol{L}_{\bar{f}}\boldsymbol{w}\right)+\boldsymbol{s}^{\mathrm{T}}\boldsymbol{M}(\boldsymbol{w})(\boldsymbol{\tau}-\boldsymbol{I})\boldsymbol{u}_n\\&\quad+\boldsymbol{s}^{\mathrm{T}}\boldsymbol{M}(\boldsymbol{w})\boldsymbol{v}-\boldsymbol{s}^{\mathrm{T}}\boldsymbol{\tau}\boldsymbol{k}_1\boldsymbol{\Xi}_1(\boldsymbol{s})-\boldsymbol{s}^{\mathrm{T}}\boldsymbol{\tau}\boldsymbol{z}_n-\boldsymbol{s}^{\mathrm{T}}\boldsymbol{\tau}\boldsymbol{\mu}_1\boldsymbol{s}+\boldsymbol{s}^{\mathrm{T}}\boldsymbol{k}_I\boldsymbol{w}\\&\quad-\boldsymbol{z}_n^{\boldsymbol{T}}\boldsymbol{\Xi}_2(\boldsymbol{s})-\boldsymbol{z}_n^{\boldsymbol{T}}\boldsymbol{k}_2^{-1}\boldsymbol{\mu}_2\boldsymbol{z}_n+\boldsymbol{s}^{\mathrm{T}}\boldsymbol{w}-\boldsymbol{w}^{\mathrm{T}}\boldsymbol{w}-\boldsymbol{\phi}(\boldsymbol{w})^{\mathrm{T}}\boldsymbol{k}_\phi\boldsymbol{w}\end{aligned} \tag{64}$$

By Assumption 3 and Eq.(25), there exist constants $L_\omega,\delta_\omega>0$ such that

$$\left\|\left(\boldsymbol{I}+\boldsymbol{k}_\phi\phi'(\boldsymbol{w})\right)\left(\frac{\partial\boldsymbol{w}}{\partial t}+\boldsymbol{L}_{\bar{f}}\boldsymbol{w}\right)+\boldsymbol{M}(\boldsymbol{w})(\boldsymbol{\tau}-\boldsymbol{I})\boldsymbol{u}_n+\boldsymbol{M}(\boldsymbol{w})\boldsymbol{v}\right\|\leq L_\omega+\delta_\omega \tag{65}$$

Substituting (65) into (64) yields

$$\begin{aligned}\dot{V}_s&=\|\boldsymbol{s}\|(L_\omega+\delta_\omega)-\boldsymbol{s}^{\mathrm{T}}\boldsymbol{\tau}\boldsymbol{k}_1\boldsymbol{\Xi}_1(\boldsymbol{s})-\boldsymbol{s}^{\mathrm{T}}\boldsymbol{\tau}\boldsymbol{z}_n-\boldsymbol{s}^{\mathrm{T}}\boldsymbol{\tau}\boldsymbol{\mu}_1\boldsymbol{s}+\boldsymbol{s}^{\mathrm{T}}\boldsymbol{k}_I\boldsymbol{w}\\&\quad-\boldsymbol{z}_n^{\boldsymbol{T}}\boldsymbol{\Xi}_2(\boldsymbol{s})-\boldsymbol{z}_n^{\boldsymbol{T}}\boldsymbol{k}_2^{-1}\boldsymbol{\mu}_2\boldsymbol{z}_n+\boldsymbol{s}^{\mathrm{T}}\boldsymbol{w}-\boldsymbol{w}^{\mathrm{T}}\boldsymbol{w}-\boldsymbol{\phi}(\boldsymbol{w})^{\mathrm{T}}\boldsymbol{k}_\phi\boldsymbol{w}\end{aligned} \tag{66}$$

For the function $\boldsymbol{\Xi}(\square)$, we use the elementwise inequality $x\tanh(x/\varepsilon)\geq|x|-\varepsilon,\forall x\in\square$, since $1+|x|^\alpha\geq1$, it follows that

$$s_i\boldsymbol{\Xi}_{1i}(s_i)=\left(1+|s_i|^\alpha\right)s_i\tanh\left(\frac{s_i}{\varepsilon_i}\right)\geq|s_i|-\varepsilon_i,i=1,...,m \tag{67}$$

In our study $m=3$, summing over $i=1,...,m$ gives

$$\begin{aligned}\boldsymbol{s}^{\mathrm{T}}\boldsymbol{\tau}\boldsymbol{k}_1\boldsymbol{\Xi}_1(\boldsymbol{s})&\geq\tau_\omega\lambda_{\min}(\boldsymbol{k}_1)\textstyle\sum_{i=1}^m\left(|s_i|-\varepsilon_i\right)\\&\geq\tau_\omega\lambda_{\min}(\boldsymbol{k}_1)\left(\|\boldsymbol{s}\|-\sqrt{m}\|\boldsymbol{\varepsilon}\|\right)\\-\boldsymbol{s}^{\mathrm{T}}\boldsymbol{\tau}\boldsymbol{k}_1\boldsymbol{\Xi}_1(\boldsymbol{s})&\leq-\tau_\omega\lambda_{\min}(\boldsymbol{k}_1)\|\boldsymbol{s}\|+\lambda_{\max}(\boldsymbol{k}_1)\sqrt{m}\|\boldsymbol{\varepsilon}\|\end{aligned} \tag{68}$$

From the definition of $\boldsymbol{\Xi}(\square)$, we have

$$-\boldsymbol{s}^{\mathrm{T}}\boldsymbol{\tau}\boldsymbol{z}_n-\boldsymbol{z}_n^{\boldsymbol{T}}\boldsymbol{\Xi}_2(\boldsymbol{s})\leq\left(1+\sqrt{m}\right)\|\boldsymbol{s}\|\|\boldsymbol{z}_n\|+2\sqrt{m}\|\boldsymbol{z}_n\| \tag{69}$$

Using Young's inequality

$$\begin{aligned}\left(1+\sqrt{m}\right)\|\boldsymbol{s}\|\|\boldsymbol{z}_n\|&\leq\frac{1}{2}\|\boldsymbol{s}\|^2+\frac{\left(1+\sqrt{m}\right)^2}{2}\|\boldsymbol{z}_n\|^2\\2\sqrt{m}\|\boldsymbol{z}_n\|&\leq\frac{1}{2}\|\boldsymbol{z}_n\|^2+2m\end{aligned} \tag{70}$$

Therefore, combining (69), (70), we have

$$-\boldsymbol{s}^{\mathrm{T}}\boldsymbol{\tau}\boldsymbol{z}_{\boldsymbol{n}}-\boldsymbol{z}_{\boldsymbol{n}}^{\boldsymbol{T}}\boldsymbol{\Xi}_2(\boldsymbol{s})-\boldsymbol{z}_{\boldsymbol{n}}^{\boldsymbol{T}}\boldsymbol{k}_2^{-1}\boldsymbol{\mu}_2\boldsymbol{z}_{\boldsymbol{n}}\le\frac{1}{2}\|\boldsymbol{s}\|^2-c_n\|\boldsymbol{z}_{\boldsymbol{n}}\|^2+2m \tag{71}$$

Define $c_n=\lambda_{\min}\left(\boldsymbol{k}_2^{-1}\boldsymbol{\mu}_2\right)-\left(2+2\sqrt{m}+m\right)\Big/2>0$.

As for the uncertainty cross term and $\boldsymbol{s}^{\mathrm{T}}\boldsymbol{k}_{\boldsymbol{I}}\boldsymbol{w}+\boldsymbol{s}^{\mathrm{T}}\boldsymbol{w}$,by young's inequality,

$$\begin{aligned}\boldsymbol{s}^{\mathrm{T}}\boldsymbol{k}_{\boldsymbol{I}}\boldsymbol{w}&\le\frac{b}{2}\|\boldsymbol{s}\|^2+\frac{\|\boldsymbol{k}_{\boldsymbol{I}}\|^2}{2b}\|\boldsymbol{w}\|^2\\ \boldsymbol{s}^{\mathrm{T}}\boldsymbol{w}&\le\frac{a}{2}\|\boldsymbol{s}\|^2+\frac{1}{2a}\|\boldsymbol{w}\|^2\end{aligned} \tag{72}$$

Thus

$$\boldsymbol{s}^{\mathrm{T}}\boldsymbol{k}_{\boldsymbol{I}}\boldsymbol{w}+\boldsymbol{s}^{\mathrm{T}}\boldsymbol{w}\le\left(\frac{a+b+\delta_\omega}{2}\right)\|\boldsymbol{s}\|^2+\left(\frac{1}{2a}+\frac{\|\boldsymbol{k}_{\boldsymbol{I}}\|^2}{2b}\right)\|\boldsymbol{w}\|^2 \tag{73}$$

Together with the negative term $-\|\boldsymbol{w}\|^2$, define the coefficient of $\|\boldsymbol{w}\|^2$ as $\boldsymbol{\Lambda}$, choose $a,b>0$

$$\boldsymbol{\Lambda}=\left(1-\frac{1}{2a}-\frac{\|\boldsymbol{k}_{\boldsymbol{I}}\|^2}{2b}\right)\boldsymbol{I}>0 \tag{74}$$

Note that $a,b>0$ are free parameters introduced by Young's inequality. Since the terms $1/2a$ and $\boldsymbol{k}_{\boldsymbol{I}}^{\boldsymbol{2}}/2b$ can be made arbitrarily small by choosing a and b sufficiently large, the condition $\boldsymbol{\Lambda}>0$ does not impose a strict upper bound on $\|\boldsymbol{k}_{\boldsymbol{I}}\|$. In practice, for any desired integral gain $\|\boldsymbol{k}_{\boldsymbol{I}}\|$, one can always satisfy this inequality by taking a,b appropriately. Hence there is no inherent conflict between stability and steady-state accuracy requirements.

Substituting (68), (71), (73) to (66), we obtain

$$\begin{aligned}\dot{V}_s\le&\left(L_\omega+\delta_\omega\right)\|\boldsymbol{s}\|-\tau_\omega\lambda_{\min}\left(\boldsymbol{k}_1\right)\|\boldsymbol{s}\|+\lambda_{\max}\left(\boldsymbol{k}_1\right)\sqrt{m}\|\boldsymbol{\varepsilon}\|+\left(\frac{a+b}{2}\right)\|\boldsymbol{s}\|^2\\&-\tau_\omega\lambda_{\min}\left(\boldsymbol{\mu}_1\right)\|\boldsymbol{s}\|^2+\frac{1}{2}\|\boldsymbol{s}\|^2-c_n\|\boldsymbol{z}_{\boldsymbol{n}}\|^2-2m-\boldsymbol{w}^T\boldsymbol{\Lambda}\boldsymbol{w}\end{aligned} \tag{75}$$

Choose parameters properly such that $c_s=\tau_\omega\lambda_{\min}\left(\boldsymbol{\mu}_1\right)-\left(a+b+1\right)/2\ge0$, then the $\|\boldsymbol{s}\|^2$ term becomes $-c_s\|\boldsymbol{s}\|^2$. Also, define $c_0=\tau_\omega\lambda_{\min}\left(\boldsymbol{k}_1\right)-L_\omega-\delta_\omega>0$ Then the $\|\boldsymbol{s}\|$ term becomes $-c_0\|\boldsymbol{s}\|$. Thus (75) becomes

$$\dot{V}_s\le-c_0\|\boldsymbol{s}\|-c_s\|\boldsymbol{s}\|^2-c_n\|\boldsymbol{z}_{\boldsymbol{n}}\|^2-\boldsymbol{w}^T\boldsymbol{\Lambda}\boldsymbol{w}+D_0 \tag{76}$$

Where $D_0=\lambda_{\max}\left(\boldsymbol{k}_1\right)\sqrt{m}\|\boldsymbol{\varepsilon}\|+2m$.

ISS Stability and convergence region. Define $W_1\left(\boldsymbol{w},\boldsymbol{z}_{\boldsymbol{n}}\right)=\boldsymbol{w}^T\boldsymbol{\Lambda}\boldsymbol{w}+c_n\|\boldsymbol{z}_{\boldsymbol{n}}\|^2\ge0$, then (76) can be written as

$$\dot{V}_s\le-c_0\|\boldsymbol{s}\|-c_s\|\boldsymbol{s}\|^2-W_1\left(\boldsymbol{w},\boldsymbol{z}_{\boldsymbol{n}}\right)+D_0 \tag{77}$$

Let $\alpha(r)=c_0r+c_sr^2$, which belongs to K_∞ since $c_0>0$ and $c_s\ge0$. Define the full-state dissipation function

$$\alpha_3\left(\boldsymbol{X}\right):=\alpha\left(\|\boldsymbol{s}\|\right)+W_1\left(\boldsymbol{w},\boldsymbol{z}_{\boldsymbol{n}}\right),\boldsymbol{X}:=\left(\boldsymbol{s},\boldsymbol{w},\boldsymbol{z}_{\boldsymbol{n}}\right) \tag{78}$$

Since $\boldsymbol{\Lambda}>0$ and $c_n>0$, $\alpha_3\left(\boldsymbol{X}\right)>0$ for all $\boldsymbol{X}\ne0$, and $\alpha_3\left(\boldsymbol{X}\right)\ge c_{\min}\|\boldsymbol{X}\|$, $c_{\min}:=\min\left\{c_0,\lambda_{\min}\left(\boldsymbol{\Lambda}\right),c_n\right\}>0$; hence α_3 is positive definite and radially unbounded in $\boldsymbol{X}$. From $\boldsymbol{e}=\boldsymbol{k}_{\boldsymbol{I}}^{-1}\left(\boldsymbol{s}-\boldsymbol{w}-\boldsymbol{k}_\phi\boldsymbol{\phi}\left(\boldsymbol{w}\right)\right)$. By the properties of $\phi(\cdot)$ and lemma 1, $\|\boldsymbol{\phi}\left(\boldsymbol{w}\right)\|\le\|\boldsymbol{w}\|$, where

$$\|\boldsymbol{e}\|\le\lambda_{\max}\left(\boldsymbol{k}_{\boldsymbol{I}}^{-1}\right)\left(\|\boldsymbol{s}\|+\left(1+\|\boldsymbol{k}_\phi\|\right)\|\boldsymbol{w}\|\right) \tag{79}$$

Substituting (79) into Lyapunov function V_s yields the upper bound $V_s\le\bar{\alpha}\left(\|\boldsymbol{X}\|\right)$ with

$$\bar{\alpha}\left(r\right):=\frac{1}{2}r^2+\frac{1}{2}\lambda_{\max}\left(\boldsymbol{k}_2^{-1}\right)r^2+\frac{1}{2}\lambda_{\max}\left(\boldsymbol{k}_{\boldsymbol{I}}\right)\lambda_{\max}^2\left(\boldsymbol{k}_{\boldsymbol{I}}^{-1}\right)\left(2+\|\boldsymbol{k}_\phi\|\right)^2r^2\in K_\infty \tag{80}$$

Conversely, since each component of $\boldsymbol{w}+\boldsymbol{k}_\phi\boldsymbol{\phi}\left(\boldsymbol{w}\right)$ has derivative $1+k_{\phi i}\phi_i'\left(w_i\right)\ge1-k_{\phi i}>0$, one has $\|\boldsymbol{w}+\boldsymbol{k}_\phi\boldsymbol{\phi}\left(\boldsymbol{w}\right)\|\ge\underline{k}\|\boldsymbol{w}\|$ with $\underline{k}:=\min_i\left(1-k_{\phi i}\right)>0$; using $\boldsymbol{w}+\boldsymbol{k}_\phi\boldsymbol{\phi}\left(\boldsymbol{w}\right)=\boldsymbol{s}-\boldsymbol{k}_{\boldsymbol{I}}\boldsymbol{e}$ and the lower bound

$$V_s \geq \frac{1}{2}\|\boldsymbol{s}\|^2 + \frac{1}{2}\lambda_{\min}\left(\boldsymbol{k}_2^{-1}\right)\|\boldsymbol{z_n}\|^2 + \frac{1}{2}\lambda_{\min}\left(\boldsymbol{k_I}\right)\|\boldsymbol{e}\|^2 \tag{81}$$

it follows that $\|\boldsymbol{X}\| \leq \sigma(V_s)$ for some $\sigma \in K_\infty$, i.e., there exists $\underline{\alpha} \in K_\infty$ with $\underline{\alpha}(\|\boldsymbol{X}\|) \leq V_s$. From (77)-(78) and (80), $\|\boldsymbol{X}\| \geq \bar{\alpha}^{-1}(V_s)$ implies $\alpha_3(\boldsymbol{X}) \geq c_{\min}\bar{\alpha}^{-1}(V_s) := \alpha_4(V_s)$ with $\alpha_4 \in K$; hence

$$\dot{V}_s \leq -\alpha_4(V_s) + D_0 \tag{82}$$

Applying the comparison lemma to (82) and invoking the standard ISS Lyapunov characterization, there exist $\beta \in KL$ and $\gamma \in K$ such that, for all $t \geq 0$,

$$\|\boldsymbol{X}\| \leq \beta\left(\|\boldsymbol{X}(0)\|, t\right) + \gamma(D_0) \tag{83}$$

Hence the closed-loop system is ISS with respect to the lumped fault-disturbance bound D_0. Moreover, (83) with (79) shows that $\boldsymbol{e}$ is ultimately bounded by a class-K function of D_0, so the boundedness of the integral state closes automatically.

From (76), $\dot{V}_s < 0$ whenever $\alpha_3(\boldsymbol{X}) > D_0$; since α_3 is radially unbounded, the sublevel set

$$\begin{aligned}\Omega &= \left\{\boldsymbol{X} : \alpha_3(\boldsymbol{X}) \leq D_0\right\} \\ &= \left\{(\boldsymbol{s}, \boldsymbol{w}, \boldsymbol{z_n}) : c_0\|\boldsymbol{s}\| + c_s\|\boldsymbol{s}\|^2 + \boldsymbol{w}^T\boldsymbol{\Lambda}\boldsymbol{w} + c_n\|\boldsymbol{z_n}\|^2 \leq D_0\right\}\end{aligned} \tag{84}$$

is compact, forward invariant in the limit, and globally attractive, i.e., the trajectories converge asymptotically to Ω. Since $W_1 \geq 0$, (84) necessarily implies $c_0\|\boldsymbol{s}\| + c_s\|\boldsymbol{s}\|^2 \leq D_0$; If $c_s > 0$, solving the quadratic inequality yields $\|\boldsymbol{s}\| \leq \left(-c_0 + \sqrt{c_0^2 + 4c_sD_0}\right)\Big/2c_s$, if $c_s = 0$, then $\|\boldsymbol{s}\| \leq D_0/c_0$.

Finally, when $\boldsymbol{s} \to \Omega$, the key variable $\boldsymbol{w} = \boldsymbol{g}_2^{\mathrm{T}}\left[\partial V/\partial \boldsymbol{x}_2\right]^{\mathrm{T}}$ satisfies $\|\boldsymbol{w}\| \leq \sigma(V_s) \leq \sigma\left(\alpha_4^{-1}(D_0)\right)$; since the map $\partial V/\partial \boldsymbol{x}_2 \mapsto \boldsymbol{g}_2^{\mathrm{T}}\left[\partial V/\partial \boldsymbol{x}_2\right]^{\mathrm{T}}$ is radially unbounded (by the radial unboundedness of the nominal Lyapunov function V and the invertibility of g_2), $\partial V/\partial \boldsymbol{x}_2$, and hence the closed-loop states, converge to a neighborhood of the origin whose size is governed by $\gamma(D_0)$.

This concludes the proof.

In conclusion, the SMLR framework has been rigorously established. The nonlinear sliding surface design coupled with the finite-time nominal controller not only accelerates convergence of the sliding variable as it approaches the neighborhood of zero, but also effectively suppresses chattering through the boundary layer. Furthermore, the fault-tolerant controller preserves control signal continuity while significantly enhancing robustness against actuator faults, with the ultimate bound explicitly characterized in Theorem 2. These theoretical advantages will be comprehensively validated through numerical simulations in Section 4, demonstrating superior tracking performance and fault accommodation capabilities compared to conventional approaches.

Remark 7. The explicit arguments of the Lyapunov function V_s are $(\boldsymbol{s}, \boldsymbol{w}, \boldsymbol{e})$, whereas the dissipation rate and the convergence set are expressed in $(\boldsymbol{s}, \boldsymbol{w}, \boldsymbol{z_n})$; their consistency is established by the two-sided K_∞ bounds $\underline{\alpha}(\|\boldsymbol{X}\|) \leq V_s \leq \bar{\alpha}(\|\boldsymbol{X}\|)$. The physical origin of this equivalence lies in the integral structure of the sliding surface. The integral state $\boldsymbol{e}$ is an algebraic function of $(\boldsymbol{s}, \boldsymbol{w})$ rather than an independent degree of freedom, so the true state dimension of the closed-loop system is $(\boldsymbol{s}, \boldsymbol{w}, \boldsymbol{z_n})$. Without this equivalence, scenarios such as bounded V_s with unbounded $\boldsymbol{w}$, or divergent $\boldsymbol{e}$ undetected by the dissipation terms, could arise, invalidating both the ISS and the invariance arguments. This remark confirms that no state direction is neglected in the proposed proof.

Remark 8. The ultimate bound for the sliding variable $\boldsymbol{s}$ given after (84) is derived by projecting the joint invariant set Ω onto the $\boldsymbol{s}$-subspace. It represents a conservative but strictly rigorous upper bound. In physical reality, the dissipation function $\alpha_3(\boldsymbol{X})$ contains the term $\boldsymbol{w}^T\boldsymbol{\Lambda}\boldsymbol{w}$. Since $\boldsymbol{w}$ is the Lyapunov Redesign key variable related to the angular rate tracking errors, the controller will simultaneously drive both $\boldsymbol{s}$ and $\boldsymbol{w}$ towards the origin. Therefore, the actual steady-state error of $\boldsymbol{s}$ is typically much smaller than the worst-case bound D_0/c_0, which is validated by the numerical simulations.

4. Numerical simulation

To verify the effectiveness and the superior performance of the SMLR for fault-tolerant control of morphing aircraft proposed in this paper. Numerical simulations are carried out and divided into four cases. The first case verifies the nominal controller during the morphing process. The second verifies the SMLR under different actuator fault conditions. Subsequently, comparative simulations of different LR-based fault-tolerant methods and AFTC method are conducted, demonstrating the superiority of the proposed method. Finally, programmed angle commands with coefficient perturbations are adopted to verify robustness.

4.1. Nominal Controller Validation

This section presents the nominal case simulation (without actuator faults) to verify the nominal controller and provide a basic analysis of the control strategy. The initial conditions are $V_0 = 200m/s, H_0 = 5.42km, \alpha_0 = \gamma_{V0} = 0^\circ, \beta_0 = 2^\circ$, initial angular rates are zero and initial morphing ratio is 1, the simulation step is $dt = 0.01s$ .The parameters of nominal controller are given in Table 1.

Table 1 Parameters of nominal controller.

Parameter	Value	Parameter	Value
r_1, r_2, r_3	0.5,0.5,0.5	m_{21}, m_{22}, m_{23}	12,3,12
m_{11}, m_{12}, m_{13}	16,8,16	l_{21}, l_{22}, l_{23}	5,2,5
l_{11}, l_{12}, l_{13}	2,1,2	$k_{f21}, k_{f22}, k_{f23}$	0.25,0.25,0.25
$k_{f11}, k_{f12}, k_{f12}$	1,1,1	μ_f	0.01

The numerical simulation results in this section are shown in the figures below.

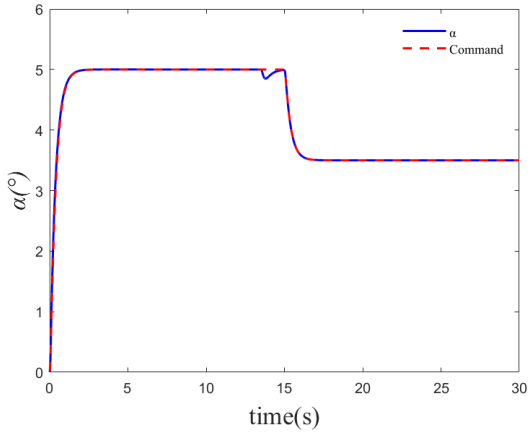


Fig. 2. Curves of attack angle in nominal case

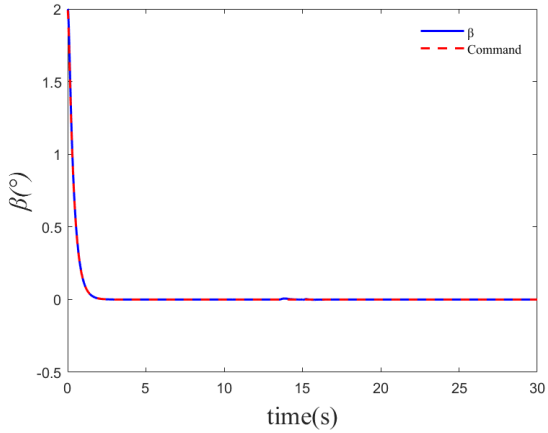


Fig. 3. Curves of sideslip angle in nominal case

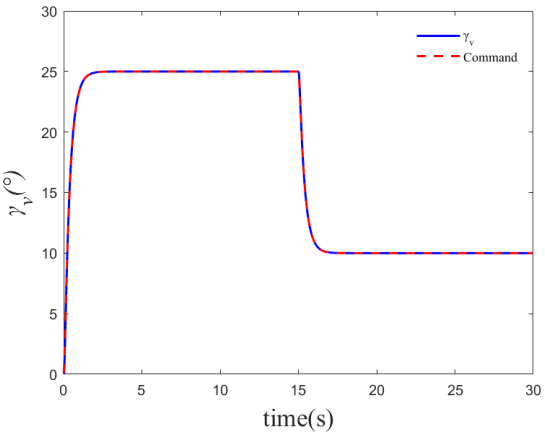


Fig. 4. Curves of bank angle in nominal case

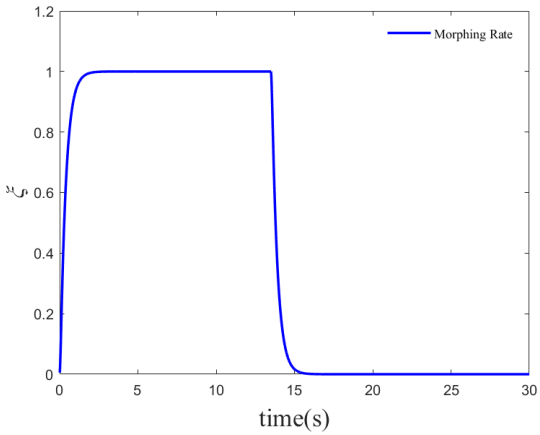


Fig. 5. Curves of morphing rate in nominal case

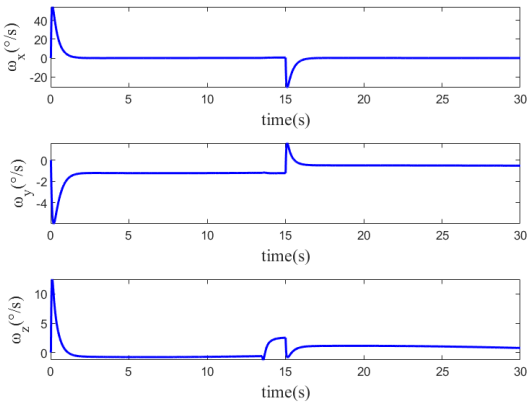


Fig. 6. Curves of angular rates in nominal case

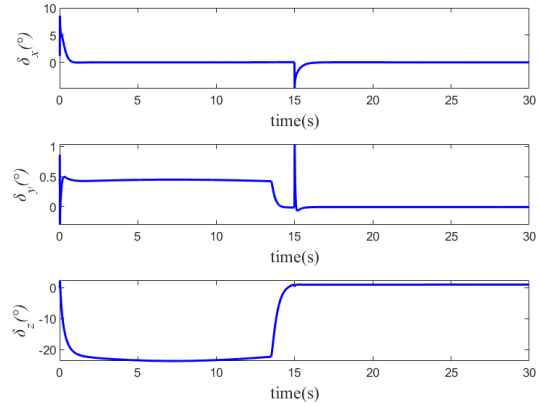


Fig. 7. Curves of rudder deflection angles in nominal case

From Fig. 2 to Fig. 7 show the results of simulation for the nominal case. It can be observed that the nominal controller achieves satisfactory tracking performance. Fig. 2,Fig. 3 and Fig. 4 present the curves of attack angle, sideslip angle, and bank angle. In the nominal case, the attitude angles track the given commands effectively. Although the morphing process shown in Fig. 5 induces bounded steady-state errors, the controller maintains rapid and accurate response. Moreover, Fig. 6 and Fig. 7 further display the angular rates and rudder deflections, illustrating the effects of morphing and command variations. The morphing process gradually alters the aerodynamic characteristics, inducing incremental adjustments in the rudder deflections from approximately 13s onward. In contrast, command changes cause abrupt variations in the rudder deflections at 15s, all within the admissible actuation range.

Above analysis demonstrates the effectiveness of the nominal controller, providing a fundamental basis for subsequent verification of the fault-tolerant controller.

4.2. Fault-Tolerant Controller Validation

This section evaluates the proposed method under three actuator fault scenarios to verify its effectiveness and response speed. The nominal controller's performance under the corresponding fault in Case 3 is also included for comparison. The initial conditions and controller parameters remain consistent with section 4.1, with the simulation step size still set at 0.01s. Additionally, All faults are injected within 10s-25s, the fault conditions are listed below

Table 2 Three different actuator fault cases.

Case	Fault
Case 1	$\boldsymbol{\tau} = diag([0.5+0.2\sin(\pi t/2), 0.8, 0.6+0.2\cos(\pi t/2)]), 20s \le t \le 25s$ $\boldsymbol{\upsilon} = [1.6+0.5\sin(\pi t/5), 0.8, -1.2+0.5\cos(\pi t/5)]^{\mathrm{T}}, 10s \le t \le 20s$
Case 2	$\boldsymbol{\tau} = diag([0.6+0.15\sin(\pi t/2), 0.9, 0.7+0.15\cos(\pi t/2)]), 20s \le t \le 25s$ $\boldsymbol{\upsilon} = [1.2+0.4\sin(\pi t/5), 0.6, -0.8+0.4\cos(\pi t/5)]^{\mathrm{T}}, 10s \le t \le 20s$
Case 3	$\boldsymbol{\tau} = diag([0.7+0.1\sin(\pi t/2), 1.0, 0.8+0.1\cos(\pi t/2)]), 20s \le t \le 25s$ $\boldsymbol{\upsilon} = [0.8+0.3\sin(\pi t/5), 0.4, -0.4+0.3\cos(\pi t/5)]^{\mathrm{T}}, 10s \le t \le 20s$

The parameters of fault-tolerant controller proposed in this paper are given in Table 3.

Table 3 Parameters of fault-tolerant controller.

Parameter	Value	Parameter	Value
$\boldsymbol{k}_{\phi}$	0.5,0.5,0.5	$\boldsymbol{\mu}_1$	35,35,35
$\boldsymbol{k}_I$	15,15,15	$\boldsymbol{k}_2$	5,5,5
α	0.85	$\boldsymbol{\mu}_2$	25,25,25
$\boldsymbol{k}_1$	80,75,75	$\boldsymbol{\varepsilon}$	0.05,0.05,0.05

The numerical simulation results in this section are shown in the figures below.

4.2.1. Verification of Assumption 3

To ensure that the bounds required in Assumption 3 are not violated during the fault-induced transients, we monitor the two quantities

$$\eta_1(t) = \left\| \left(\boldsymbol{I} + \boldsymbol{k}_{\phi}\phi'(\boldsymbol{w})\right)\left(\partial \boldsymbol{w}/\partial t + \boldsymbol{L}_{\bar{f}}\boldsymbol{w}\right) \right\|, \quad \eta_2(t) = \left\| \boldsymbol{M}(\boldsymbol{w})\left[(\boldsymbol{\tau} - \boldsymbol{I})\boldsymbol{u}_n + \boldsymbol{\upsilon}\right] \right\| \tag{85}$$

Since the fault is injected at $t = 10s$ when the aircraft has already been stabilized by the nominal control ler, we focus on the time interval $t \in [8,30]s$, which covers the entire fault-active period. The time historie s are shown in Fig. 8 and Fig. 9.

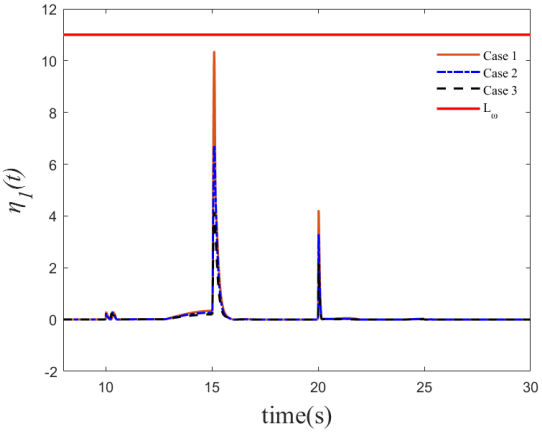


Fig. 8 Curves of the $\eta_1(t)$ in fault case

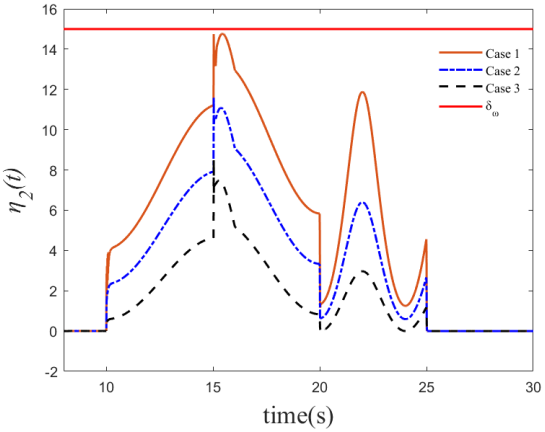


Fig. 9 Curves of the $\eta_2(t)$ in fault case

It is observed that $\eta_1(t)$ stays below 11 and $\eta_2(t)$ stays below 15 during this interval. Consequently, w e set $L_\omega = 11$ and $\delta_\omega = 15$ as the constant bounds in Assumption 3. **These conservative values are never exceeded in the fault transient**, thereby supporting the theoretical analysis that relies on Assumption 3.

4.2.2. Controller Validation

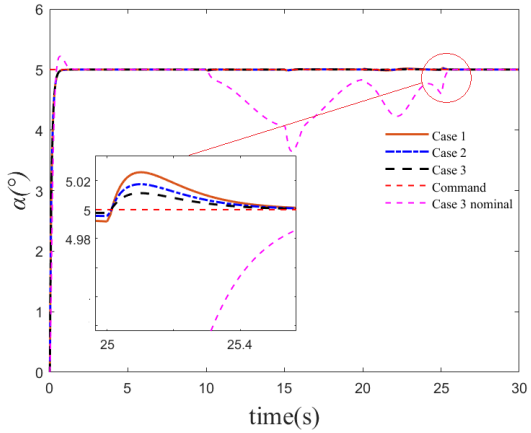


Fig. 10. Curves of the attack angle in fault case

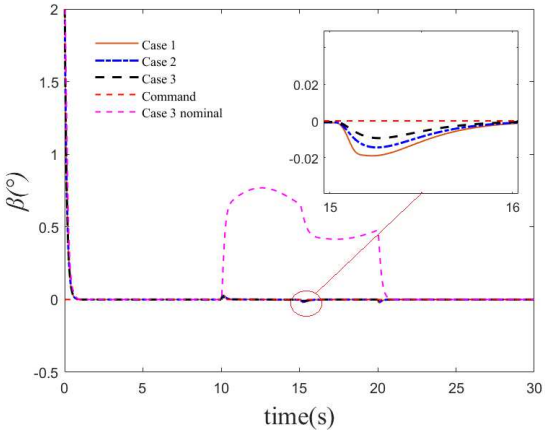


Fig. 11. Curves of the sideslip angle in fault case

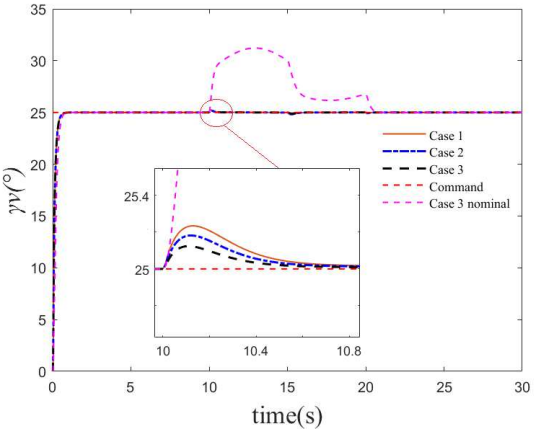


Fig. 12. Curves of the bank angle in fault case

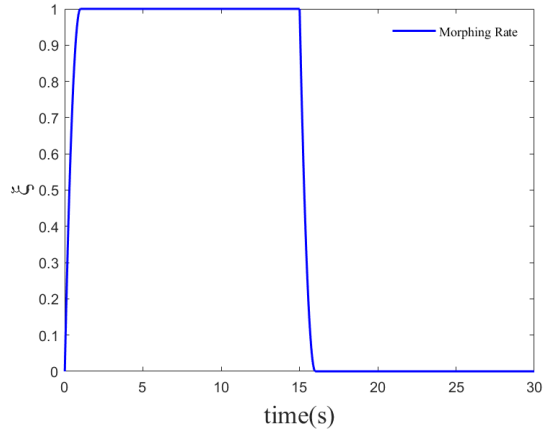


Fig. 13. Curves of the morphing rate in fault case

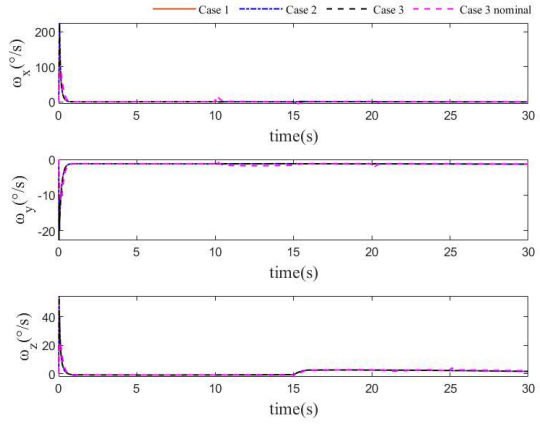


Fig. 14. Curves of the angular rates in fault case

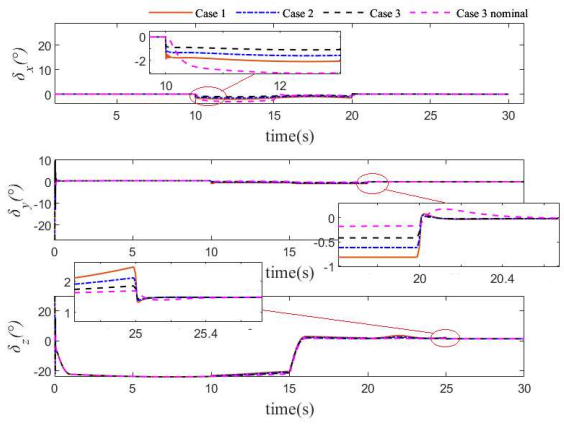


Fig. 15. Curves of the rudder deflection angles in fault case

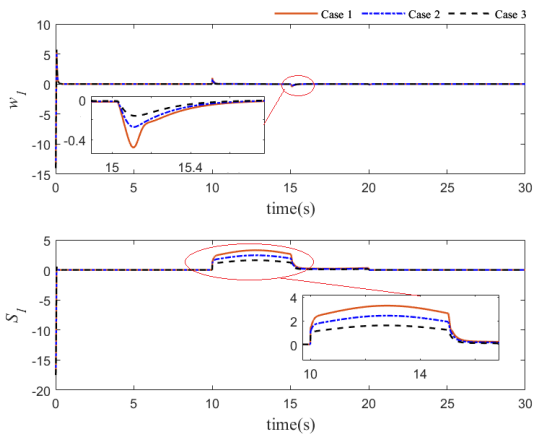


Fig. 16. Curves of w_1 and S_1 in fault case

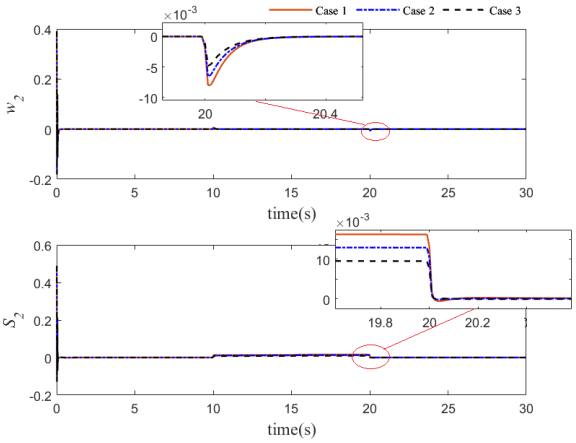


Fig. 17. Curves of w_2 and S_2 in fault case

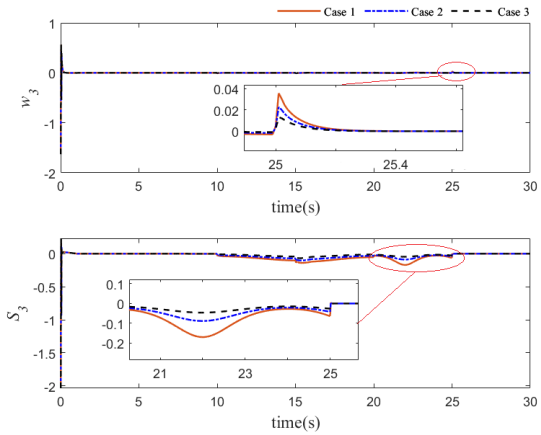


Fig. 18. Curves of w_3 and S_3 in fault case

From Fig. 10 to Fig. 18 present the simulation results under the three asymmetric and time-varying fault cases in Table 2. Despite channel-dependent control effectiveness loss and continuously time-varying drift terms (in sinusoidal or cosine form), the proposed fault-tolerant controller maintains satisfactory attitude tracking.

From Fig. 10 to Fig. 12 show the attitude angles across the three fault cases, confirming reliable attitude regulation throughout the morphing process (Fig. 13) and revealing improved tracking as fault severity decreases-demonstrating the method's adaptability. Fig. 14 and Fig. 15 show the variation of angular rates and rudder deflection angles over time. From Fig. 16 to Fig. 18 depict the key variable $\boldsymbol{w}$ and proposed nonlinear sliding mode surface $\boldsymbol{s}$, showing rapid and effective convergence of the key variable under fault conditions. A more detailed discussion on how the designed sliding surface improves convergence is provided in Section 4.3.

Overall, these results confirm the robustness of the proposed SMLR framework against realistic and challenging fault profiles, including asymmetric and time-varying actuator faults.

4.3. Fault-Tolerant Methods Comparison

To further validate the proposed SMLR (LR-NSM) framework, a comparative simulation is conducted against existing LR-based sliding-mode FTC schemes (LR-STA [45]) and LR-LCC [46]) and a representative AFTC method [47]. The results confirm that our method delivers superior fault-tolerant control performance, and that the nonlinear sliding surface offers enhanced capabilities.

The initial conditions and controller parameters are kept consistent with Sections 4.1 and 4.2, using a simulation step size of 0.01 s. Additionally, the faults occurring under different methods remain consistent, specifically as

$\boldsymbol{\tau} = diag([0.6, 0.6, 0.6]), 20s \le t \le 25s; \boldsymbol{\upsilon} = [0.8, 0.6, -0.8]^{\mathrm{T}}, 10s \le t \le 20s$.

The numerical simulation results in this section are shown in the figures below.

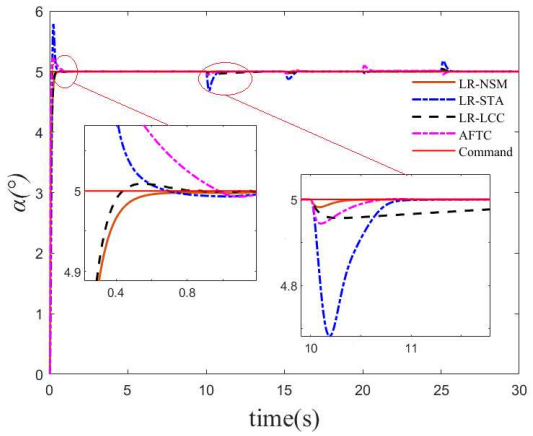


Fig. 19. Comparison curves of the attack angle

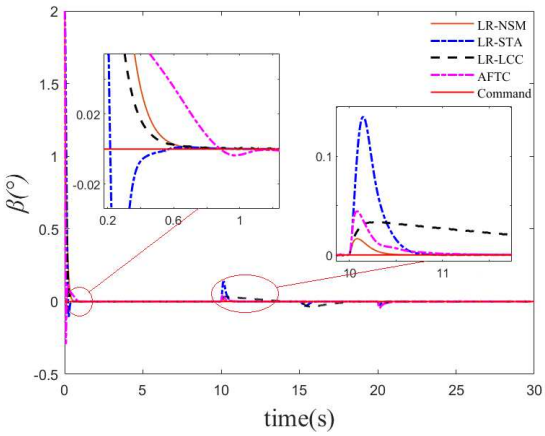


Fig. 20. Comparison curves of the sideslip angle

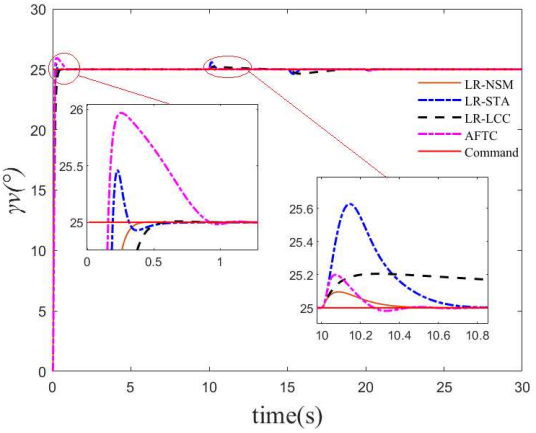


Fig. 21. Comparison curves of the bank angle

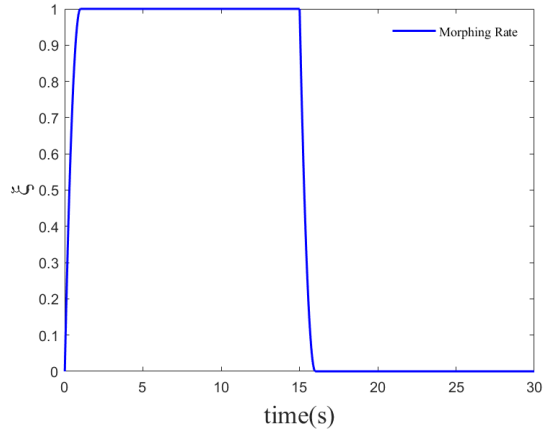


Fig. 22. Curve of the morphing rate in this case

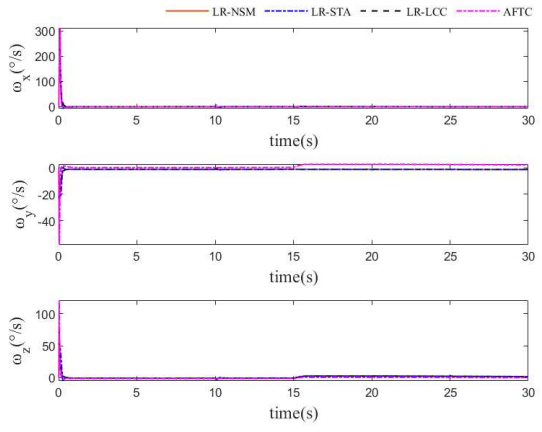


Fig. 23. Comparison curves of the angular rates

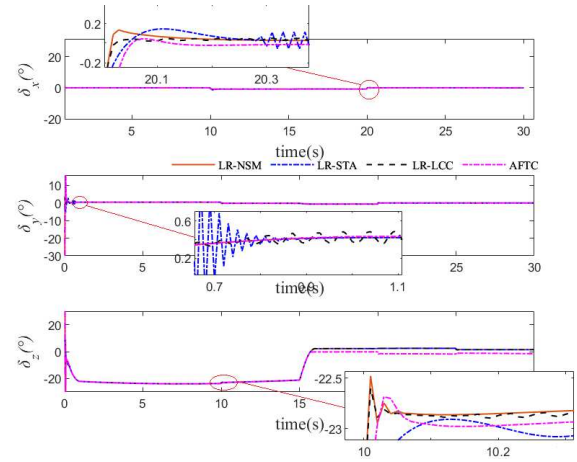


Fig. 24. Comparison curves of the rudder deflection angles

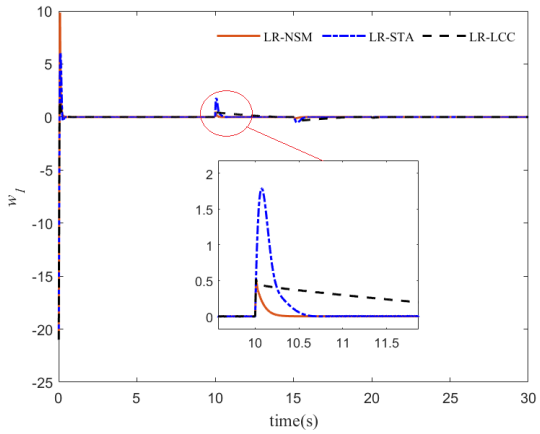


Fig. 25. Comparison curves of w_1

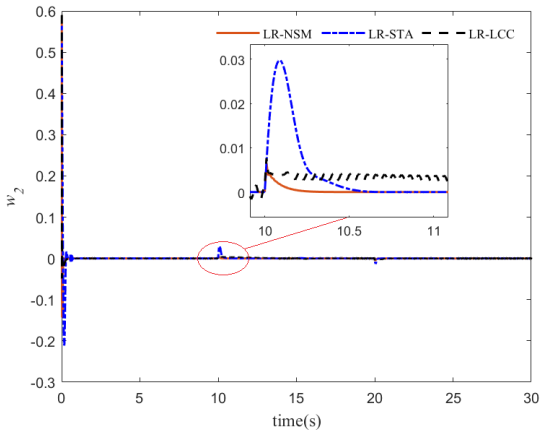


Fig. 26. Comparison curves of w_2

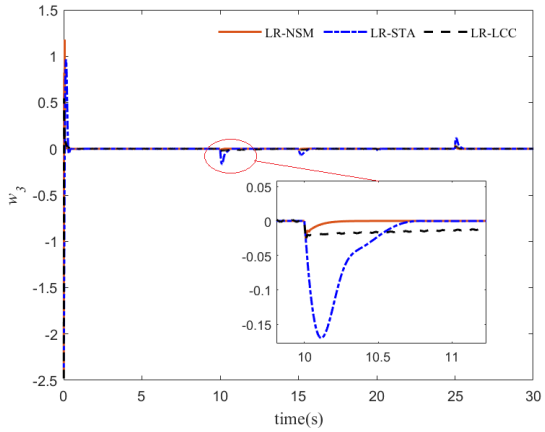


Fig. 27. Comparison curves of w_3

Table 4 Quantitative metrics of Methods

Methods	MoST/(s)	MoMAE/(deg)	MoRMSE/(deg)	MoACA/(deg)
LR-NSM	**0.41**	**0.0436**	**0.0163**	0.0076
LR-STA	0.87	0.3619	0.0496	0.0614
LR-LCC	1.42	0.1482	0.0514	0.0447
AFTC	0.70	0.1161	0.0153	**0.0073**

To provide a quantitative assessment of the control performance and chattering suppression capability, all metrics are averaged over the three attitude channels and computed over the fault-active interval(10-25 s): mean of settling time (ST), mean of maximum absolute error (MAE), mean of root mean square error (RMSE), mean of average chattering amplitude(ACA). The results are summarized in Table 4.

The proposed LR-NSM achieves the best performance across tracking and smoothness indices. Specifically, it yields the smallest RMSE and the shortest ST, indicating substantially faster fault recovery. In terms of chattering suppression, LR-NSM attains an ACA of only 0.0076 deg, representing a big reduction relative to LR-STA and LR-LCC. Notably, this chattering level is comparable to that of the AFTC method (ACA=0.0073 deg), despite LR-NSM requiring no fault detection and diagnosis module. These quantitative results demonstrate that the proposed scheme simultaneously improve tracking precision, transient recovery speed, and chattering suppression.

Fig. 19-Fig. 27 display the simulation results for the different methods. The proposed method exhibits faster response and higher control accuracy under faults, with smoother control signal transitions and effectively suppressed chattering.

Fig. 19-Fig. 21 present the attitude angle responses. All methods maintain fault-tolerant control under fault conditions. Compared with STA and LCC, our method shows a quicker response and higher accuracy during faults. It also achieves excellent steady-state fault accommodation, with tracking errors similar in magnitude to those of the AFTC

method, highlighting the high fault tolerance of both strategies. However, during the initial phase (0-5 s) and immediately after fault onset, the AFTC method exhibits larger transient tracking errors and longer settling times. This stems from the convergence process of the neural network observer: without prior fault information, the observer requires a finite amount of time to build an accurate estimate of the lumped uncertainty, during which the control compensation is suboptimal. In contrast, the proposed NSM provides instantaneous robust compensation without any learning phase, leading to smoother transients. The control effort (rudder deflections) of the AFTC method remains comparable to that of NSM after convergence, indicating that the PFTC approach incurs no significant control energy penalty despite its fixed-gain robust design.

Fig. 23 and Fig. 24 indicate that all methods generate continuous control signals. It is apparent that the proposed NSM and AFTC method yields smoother control signals than the STA method and faster response compared to the LCC method. From Fig. 25 to Fig. 27 show the curves of key variable $\boldsymbol{w}$ of different methods. A direct comparison reveals that the proposed method achieves faster convergence of the key variables and higher convergence accuracy under fault conditions.

Overall, the results demonstrate that the proposed PFTC scheme achieves competitive fault-tolerance performance compared with the AFTC benchmark, while offering the additional practical advantages of simpler structure, no need for fault diagnosis, and superior transient behavior at the very beginning of operation and immediately after fault occurrence.

4.4. Robustness Validation

This section assesses the robustness of the proposed method against aerodynamic coefficient perturbations. Given that aerodynamic discrepancies are inevitable during the cross-domain flight of morphing aircraft, the scheme's resilience must be evaluated under concurrent actuator faults and parametric uncertainties. To this end, programmed attitude commands with injected coefficient perturbations are employed. Compound disturbances are introduced by simultaneously perturbing the three-axis moment coefficients and the atmospheric density, as detailed in Table 5.

Table 5 Aerodynamic parameters perturbation table

ρ	m_z	m_y	m_x
+20%	+30%	+30%	+30%
			-30%
		-30%	+30%
			-30%
	-30%	+30%	+30%
			-30%
		-30%	+30%
			-30%
-20%	+30%	+30%	+ 30%
			-30%
		-30%	+30%
			-30%
	-30%	+30%	+30%
			-30%
		-30%	+30%
			-30%

In this section, the initial conditions and controller parameters remain consistent with section 4.1 and section 4.2. The simulation step size still set at 0.01s with faults: $\boldsymbol{\tau} = diag([0.5, 0.5, 0.5]), 15s \le t \le 25s; \boldsymbol{\upsilon} = [1.6, 1.4, -2.0]^{\mathrm{T}}, 10s \le t \le 20s$.

The numerical simulation results in this section are shown in the figures below.

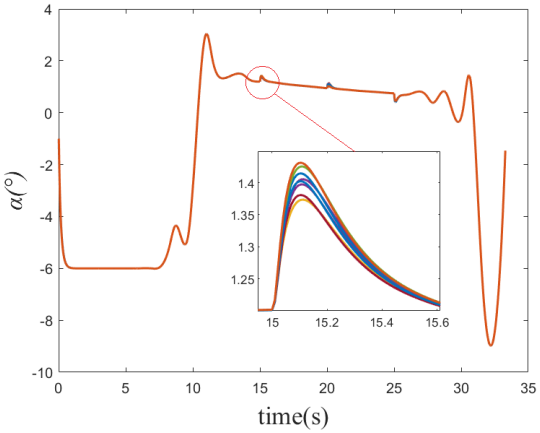


Fig. 28. Curves of attack angle under aero perturbance

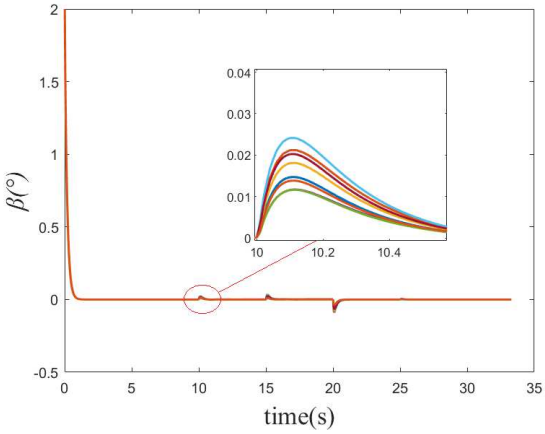


Fig. 29. Curves of sideslip angle under aero perturbance

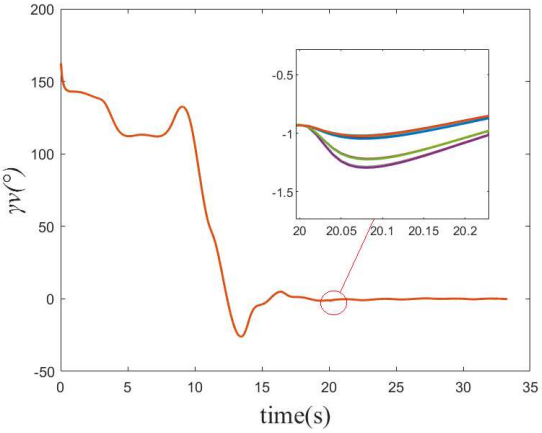


Fig. 30. Curves of bank angle under aero perturbance

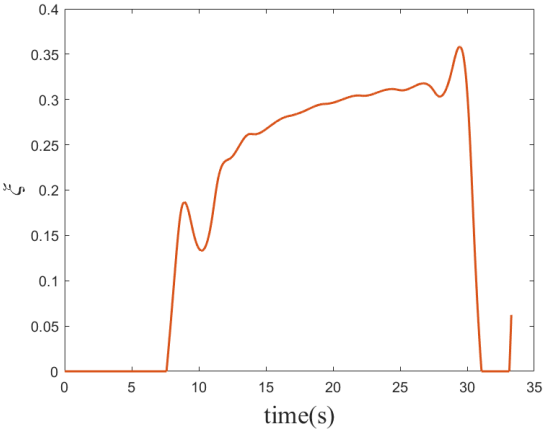


Fig. 31. Morphing rate of program angle command

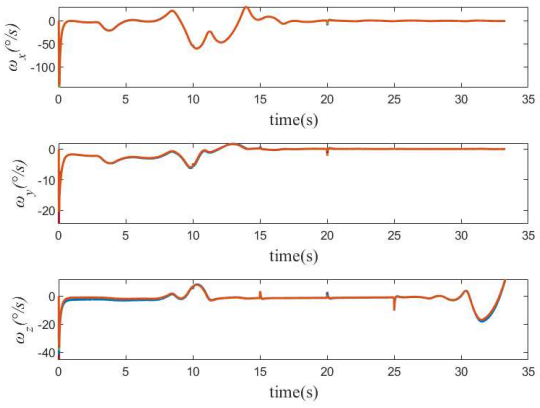


Fig. 32. Curves of angular rates under aero perturbance

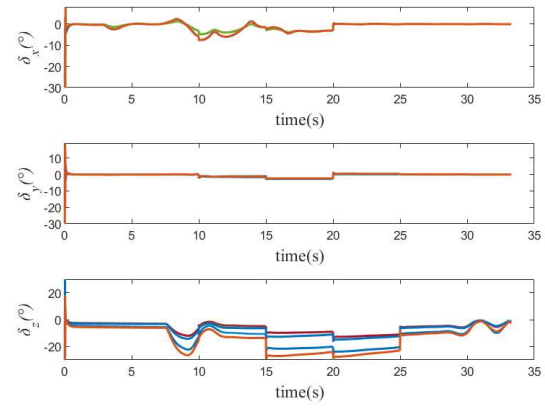


Fig. 33. Curves of rudder deflection angles under aero perturbance

Fig. 28-Fig. 33 present the simulation results under these perturbed conditions. The results confirm that the proposed method maintains high robustness to aerodynamic perturbations in the presence of actuator faults. Fig. 28-Fig. 30 depict the attitude tracking responses, while Fig. 31 shows the morphing rate. Notably, satisfactory control performance is preserved even under the combined effect of actuator faults and aerodynamic perturbations. Fig. 32 and Fig. 33 further illustrate the control signal behavior under varying perturbation levels. Collectively, these results validate the significant robustness of the proposed scheme to aerodynamic parameter variations under fault conditions.

5. Conclusions

This paper has proposed a novel sliding-mode Lyapunov redesign (SMLR) framework for fault-tolerant control of morphing aircraft. Leveraging the LR structure, the control architecture is decoupled into a nominal controller and a fault-tolerant compensator. A finite-time nominal controller is designed to guarantee rapid convergence under fault-free conditions, establishing the baseline for the subsequent fault-tolerant design. For fault accommodation, a nonlinear sliding surface formulated in terms of the LR key variable is introduced, and a continuous sliding mode control law is derived. The input-to-state stability (ISS) of the resulting closed-loop system is rigorously proved via Lyapunov theory. Step commands and programmed attitude commands are employed to demonstrate the control performance. Simulation results confirm that the system achieves rapid and precise attitude tracking throughout the continuous morphing process and under actuator faults. The proposed sliding surface ensures fast, high-accuracy convergence of the key variables, in full agreement with the theoretical analysis. Moreover, the method exhibits pronounced robustness to aerodynamic parameter perturbations under actuator faults.

Besides, future work may pursue several directions. First, a standard anti-windup mechanism can be incorporated into the integral term of the sliding surface to prevent windup under prolonged faults. Second, an adaptation mechanism could be integrated to enable automatic online parameter tuning. Third, the proposed SMLR methodology may be extended to handle sensor and communication faults, for instance by combining robust observers or delay-compensation techniques. Addressing these issues would broaden the applicability of the SMLR framework and strengthen its practical value for safety-critical aerospace systems.

Author contributions HH: Conceptualization, Methodology, Writing—original draft preparation; WP: Conceptualization, investigation, Writing—review and editing, Supervision; TGJ: Funding acquisition, Supervision.

Funding This work is supported by National Natural Science Foundation of China (Grant Numbers 92371203).

Data availability No datasets were generated or analyzed during the current study.

Declarations

Conflict of interest The authors have no conflict of interest to declare that are relevant to the content of this article.

References

[1] L. CHU, Q. LI, F. GU, X. DU, Y. HE, Y. DENG, Design, modeling, and control of morphing aircraft: A review, Chin. J. Aeronaut. 35 (2022) 220–246. https://doi.org/10.1016/j.cja.2021.09.013.

[2] M.S. PARANCHEERIVILAKKATHIL, J.S. PILAKKADAN, R.M. AJAJ, M. AMOOZGAR, D. ASADI, Y. ZWEIRI, M.I. FRISWELL, A review of control strategies used for morphing aircraft applications, Chin. J. Aeronaut. 37 (2024) 436–463. https://doi.org/10.1016/j.cja.2023.12.035.

[3] R.M. Ajaj, M.S. Parancheerivilakkathil, M. Amoozgar, M.I. Friswell, W.J. Cantwell, Recent developments in the aeroelasticity of morphing aircraft, Prog. Aerosp. Sci. 120 (2021) 100682. https://doi.org/10.1016/j.paerosci.2020.100682.

[4] J. Zhang, A.D. Shaw, C. Wang, H. Gu, M. Amoozgar, M.I. Friswell, B.K.S. Woods, Aeroelastic model and analysis of an active camber morphing wing, Aerosp. Sci. Technol. 111 (2021) 106534. https://doi.org/10.1016/j.ast.2021.106534.

[5] A. Syed, M. Moshtaghzadeh, D. Hodges, P. Mardanpour, Aeroelasticity of Flying Wing Aircraft Subject to Morphing-A Stability Study, AIAA Journal (2022). https://doi.org/10.2514/1.J061574.

[6] C. HE, F. ZHAN, L. MA, G. CHEN, J. MA, Aero-structural design of joined-wing aircraft based on high-fidelity model, Chin. J. Aeronaut. 37 (2024) 363–377. https://doi.org/10.1016/j.cja.2023.10.029.

[7] Z. YU, Y. ZHANG, B. JIANG, J. FU, Y. JIN, A review on fault-tolerant cooperative control of multiple unmanned aerial vehicles, Chin. J. Aeronaut. 35 (2022) 1–18. https://doi.org/10.1016/j.cja.2021.04.022

[8] G. Yao, Y. Li, H. Zhang, Y. Jiang, T. Wang, F. Sun, X. Yang, Review of hybrid aquatic-aerial vehicle (HAAV): Classifications, current status, applications, challenges and technology perspectives, Prog. Aerosp. Sci. 139 (2023) 100902. https://doi.org/10.1016/j.paerosci.2023.100902.

[9] M.N. Hasan, M. Haris, S. Qin, Fault-tolerant spacecraft attitude control: A critical assessment, Prog. Aerosp. Sci. 130 (2022) 100806. https://doi.org/10.1016/j.paerosci.2022.100806.

[10] W. Li, X. Han, Y. Zhi, B. Wang, L. Liu, H. Fan, Adaptive finite-time incremental backstepping fault-tolerant control for flying-wing aircraft with state constraints, Aerosp. Sci. Technol. 147 (2024) 108968. https://doi.org/10.1016/j.ast.2024.108968.

[11] Y. Li, T. Wang, X. Liu, C. -y. Wen, Predefined-Time Active Fault-Tolerant Control of Transport Aircraft Subject to Control Surface Failures, IEEE Trans. Aerosp. Electron. Syst. 61 (2025) 5731–5744. https://doi.org/10.1109/TAES.2024.3523878.

[12] M. Sato, A. Marcos, D. Akasaka, Design of structured H∞ flight controllers: Passive fault-tolerant versus observer-based structures, ISA Trans. 143 (2023) 20–37. https://doi.org/10.1016/j.isatra.2023.08.029.

[13] H. Xiao, Z. Zhen, Y. Xue, Fault-tolerant attitude tracking control for carrier-based aircraft using RBFNN-based adaptive second-order sliding mode control, Aerosp. Sci. Technol. 139 (2023) 108408. https://doi.org/10.1016/j.ast.2023.108408.

[14] J. Zhu, G. Yang, W. Zhang, L. Yu, Cooperative Fault Tolerant Tracking Control for Multiagent Systems: An Intermediate Estimator-Based Approach, IEEE Transactions on Cybernetics 48 (2018) 2972–2980. https://doi.org/10.1109/TCYB.2017.2753383.

[15] A. Bounemeur, M. Chemachema, General fuzzy adaptive fault-tolerant control based on Nussbaum-type function with additive and multiplicative sensor and state-dependent actuator faults, Fuzzy Sets and Systems. 468 (2023) 108616. https://doi.org/10.1016/j.fss.2023.108616.

[16] A. Abdo, J. Siam, A. Abdou, Fault Detection and Fault-Tolerant Control of Single Phasing on Three-Phase System, IEEE Transactions on Instrumentation and Measurement 74 (2025). https://doi.org/10.1109/TIM.2025.3571121.

[17] M. Fu, Z. Yu, Y. Zhang, Distributed adaptive fault-tolerant cooperative control for fixed-wing UAVs with actuator faults and input constraints, ISA Trans. 167 (2025) 29–43. https://doi.org/10.1016/j.isatra.2025.08.049.

[18] L. Ouhib, R. Kara, Actuator fault estimation and fault tolerant control for uncertain Takagi-Sugeno systems: a D-stability joint synthesis, J. Franklin. Inst. 362 (2025) 107884. https://doi.org/10.1016/j.jfranklin.2025.107884.

[19] G. Guo, S. Xiao, F. Chen, Z. Hou, H. Tan, Dynamic event-triggered predefined-time adaptive attitude fault-tolerant control for uncertain unmanned aerial vehicles with disturbances and actuator faults, Aerosp. Sci. Technol. 165 (2025) 110481. https://doi.org/10.1016/j.ast.2025.110481.

[20] G. Leitmann, Guaranteed Asymptotic Stability for Some Linear Systems With Bounded Uncertainties, J. Dyn. Sys., Meas., Control. 101 (1979) 212–216. https://doi.org/10.1115/1.3426427.

[21] S. Gutman, Uncertain dynamical systems--A Lyapunov min-max approach, IEEE Trans. Automat. Contr. 24 (1979) 437–443. https://doi.org/10.1109/TAC.1979.1102073.

[22] M. Corless, Control of Uncertain Nonlinear Systems, J. Dyn. Sys., Meas., Control. 115 (1993) 362-372. https://doi.org/10.1115/1.2899076.

[23] M. Corless, G. Leitmann, Continuous state feedback guaranteeing uniform ultimate boundedness for uncertain dynamic systems, IEEE Trans. Automat. Contr. 26 (1981) 1139–1144. https://doi.org/10.1109/TAC.1981.1102785.

[24] S. Azizi, Sufficient LMI conditions and Lyapunov redesign for the robust stability of a class of feedback linearized dynamical systems, ISA Trans. 68 (2017) 90–98. https://doi.org/10.1016/j.isatra.2017.02.017.

[25] O. -J. Santos-Sánchez, R. -E. Velasco-Rebollo, L. Rodríguez-Guerrero, J. -P. Ordaz-Oliver, C. Cuvas-Castillo, Lyapunov Redesign for Input and State Delays Systems by Using Optimal Predictive Control and Ultimate Bound Approaches: Theory and Experiments, IEEE Transactions on Industrial Electronics 68 (2021) 12575–12583. https://doi.org/10.1109/TIE.2020.3040678.

[26] M. Baradaran-nia, G. Alizadeh, S. Khanmohammadi, B.F. Azar, Backstepping-based Lyapunov redesign control of hysteretic single degree-of-freedom structural systems, Nonlinear Dyn. 73 (2013) 1165–1186. https://doi.org/10.1007/s11071-013-0860-5.

[27] G. Guo, R. Zhang, Lyapunov Redesign-Based Optimal Consensus Control for Multi-Agent Systems With Uncertain Dynamics, IEEE Transactions on Circuits and Systems II: Express Briefs 69 (2022) 2902–2906. https://doi.org/10.1109/TCSII.2022.3149911.

[28] C. De Persis, R. Postoyan, A Lyapunov Redesign of Coordination Algorithms for Cyber-Physical Systems, IEEE Trans. Automat. Contr. 62 (2017) 808–823. https://doi.org/10.1109/TAC.2016.2565062.

[29] J. Xu, L.M. Fridman, E. Fridman, Y. Niu, Output-feedback Lyapunov redesign of uncertain systems with delayed measurements, International Journal of Robust and Nonlinear Control 31 (2021) 3747–3766. https://doi.org/10.1002/rnc.5464.

[30] W. Wang, G. Mengali, A. A. Quarta, H. Baoyin, Spacecraft Relative Motion Control Near an Asteroid With Uncertainties: A Lyapunov Redesign Approach, IEEE Trans. Aerosp. Electron Syst. 60 (2024) 4507–4517. https://doi.org/10.1109/TAES.2024.3378196.

[31] B. Wang, Y. Shen, N. Li, Y. Zhang, Z. Gao, An adaptive sliding mode fault-tolerant control of a quadrotor unmanned aerial vehicle with actuator faults and model uncertainties, International Journal of Robust and Nonlinear Control 33 (2023) 10182–10198. https://doi.org/10.1002/rnc.6631.

[32] F. Lin, G. Xue, S. Li, H. Liu, Y. Pan, J. Cao, Finite-time sliding mode fault-tolerant neural network control for nonstrict-feedback nonlinear systems, Nonlinear Dyn. 111 (2023) 17205–17227. https://doi.org/10.1007/s11071-023-08767-2.

[33] D. Tong, C. Xu, Q. Chen, W. Zhou, Y. Xu, Sliding mode control for nonlinear stochastic systems with Markovian jumping parameters and mode-dependent time-varying delays, Nonlinear Dyn. 100 (2020) 1343–1358. https://doi.org/10.1007/s11071-020-05597-4.

[34] A. Mousavi, A. H. D. Markazi, A. Ferrara, A Barrier-Function-Based Second-Order Sliding Mode Control With Optimal Reaching for Full-State and Input-Constrained Nonlinear Systems, IEEE Trans. Automat. Contr. 69 (2024) 395–402. https://doi.org/10.1109/TAC.2023.3263076.

[35] H. Ríos, M. Mera, A. Polyakov, A novel second-order sliding-mode controller for uncertain double integrator dynamics, Automatica 173 (2025) 112036. https://doi.org/10.1016/j.automatica.2024.112036.

[36] C. D. Cruz-Ancona, M. A. Estrada, L. Fridman, Barrier Function-Based Adaptive Lyapunov Redesign for Systems Without A Priori Bounded Perturbations, IEEE Trans. Automat. Contr. 67 (2022) 3851–3862. https://doi.org/10.1109/TAC.2021.3107453.

[37] M. A. Estrada, L. Fridman, J. A. Moreno, Passive Fault-Tolerant Control via Sliding-Mode-Based Lyapunov Redesign, IEEE Trans. Automat. Contr. 69 (2024) 6777–6788. https://doi.org/10.1109/TAC.2024.3382608.

[38] M. A. Gomez, C. D. Cruz-Ancona, L. Fridman, Super Twisting Based Lyapunov Redesign for Uncertain Linear Delay Systems, IEEE Trans. Automat. Contr. 68 (2023) 1107–1113. https://doi.org/10.1109/TAC.2022.3148309.

[39] C. Dong, Y. Liu, Q. Wang, Barrier Lyapunov function based adaptive finite-time control for hypersonic flight vehicles with state constraints, ISA Trans. 96 (2020) 163–176. https://doi.org/10.1016/j.isatra.2019.06.011.

[40] C. Bao, P. Wang, G. Tang, Integrated Guidance and Control for Hypersonic Morphing Missile Based on Variable Span Auxiliary Control, International Journal of Aerospace Engineering 2019 (2019) 6413410.

https://doi.org/10.1155/2019/6413410.

[41] K. Zimenko, A. Polyakov, D. Efimov, On finite-time robust stabilization via nonlinear state feedback, International Journal of Robust and Nonlinear Control 28 (2018) 4951–4965. https://doi.org/10.1002/rnc.4292.

[42] X. Yu, M. Zhihong, Fast terminal sliding-mode control design for nonlinear dynamical systems, IEEE Trans. Circuits Syst. I, 49(2002) 261–264. doi: 10.1109/81.983876.

[43] S.P. Bhat, D.S. Bernstein, Finite-Time Stability of Continuous Autonomous Systems., SIAM J. Control. Optim. 38 (2000) 751–766. https://doi.org/10.1137/S0363012997321358.

[44] D. Swaroop, J. K. Hedrick, P. P. Yip and J. C. Gerdes, Dynamic surface control for a class of nonlinear systems, IEEE Trans. Automat. Contr., 45(2000), 1893-1899. doi: 10.1109/TAC.2000.880994.

[45] J. A. Moreno, H. Ríos, L. Ovalle, L. Fridman, Multivariable Super-Twisting Algorithm for Systems With Uncertain Input Matrix and Perturbations, IEEE Trans. Automat. Contr. 67 (2022) 6716–6722. https://doi.org/10.1109/TAC.2021.3130880.

[46] C. A. Martínez-Fuentes, R. Seeber, L. Fridman, J. A. Moreno, Saturated Lipschitz Continuous Sliding Mode Controller for Perturbed Systems With Uncertain Control Coefficient, IEEE Trans. Automat. Contr. 66 (2021) 3885–3891. https://doi.org/10.1109/TAC.2020.3034872.

[47] Y. Li, M. Wang, Q. Xia, Back-stepping fault-tolerant control method of morphing aircraft based on fixed-time neural network observer, J. Aerosp. Eng., 38(2025), 04024119. doi/10.1061/JAEEEZ.ASENG-5700.